(31) Rundle, R. E. *J. Am. Chem. Soc.* **1957**, *79*, 3372.
(32) Engberg, A. *Acta Chem. Scand.* **1970**, *24*, 3510.
(33) Wertz, D. L.; Tyvoll, J. L. *J. Inorg. Nucl. Chem.* **1974**, *36*, 3713.
(34) Agnew, N. H. *J. Polym. Sci., Polym. Chem. Ed.* **1976**, *14*, 2819.
(35) Russell, T. P.; Jérôme, R.; Charlier, P.; Foucart, M. *Macromolecules* **1988**, *21*, 1709.
(36) Sen, A.; Weiss, R. A. *Polym. Mater. Sci. Eng.* **1988**, *58*, 981.
(37) Peiffer, D. G.; Duvdevani, I.; Agarwal, P. K.; Lundberg, R. *J. Polym. Sci., Polym. Lett.* **1986**, *24*, 581.

Theory of Adsorbed Block Copolymers

M. D. Whitmore*

Department of Physics, Memorial University of Newfoundland, St. John's, Newfoundland, Canada, A1B 3X7

J. Noolandi*

Xerox Research Centre of Canada, 2660 Speakman Drive, Mississauga, Ontario, Canada, L5K 2L1

Received September 19, 1989

ABSTRACT: We present a study of adsorbed diblock copolymers, which is based on the mean-field self-consistent theory of incompressible polymer/solvent blends. We assume that one of the blocks is tightly adsorbed and model the remaining block using the formalism recently developed for crystallizable/amorphous block copolymer blends. Restricting attention primarily to near-Θ conditions, we present series of calculations describing adsorption at a single surface and adsorption on two parallel surfaces a finite distance apart. For the second case, we calculate the long-range forces acting on the two surfaces. We make quantitative comparisons with experiment for conditions corresponding to slightly good, Θ, and slightly poor solvents. We determine the thickness and shape of the polymer density profiles, obtain approximate scaling relations and the ranges of their applicability, study finite molecular weight effects, as well as the extent of the interdigitation of layers adsorbed on opposite surfaces, and show how these quantities vary as the surface separation changes. In addition, we show how the scaling of the *apparent* range of the measured long-range force can differ from the scaling of the thickness of a single adsorbed layer.

1. Introduction

Polymer adsorption, in particular, homopolymer adsorption, has been extensively studied both experimentally and theoretically. In this paper we study adsorbed block copolymers and the resulting long-range forces acting on two surfaces with adsorbed copolymers. (We do not refer to the extensive literature on adsorbed *homo*polymers in this paper.)

The system is illustrated schematically in Figure 1. One or two surfaces are immersed in solution containing copolymers, which then adsorb. We assume that one block of the copolymer adsorbs tightly but that the second block has no particular surface affinity and extends to at least some degree into the solution. It is the nonadsorbed blocks that are of primary interest here. In fact, in this paper we assume that the only significant roles of the tightly adsorbed blocks are anchoring the dangling block and partially controlling the total surface coverage. The system is thus equivalent to a collection of grafted polymers and is frequently referred to as the polymer brush.

These systems have been studied experimentally by small-angle neutron scattering,[1,2] hydrodynamic thickness measurements,[3] and Israelachvili surface forces techniques.[4-9] The experiments provide information on the shapes and sizes of the density profiles and how they vary with, for example, molecular weight and solvent quality. Here we summarize very briefly some of the scaling results that were extracted, with a view to illustrating the range of results which we attempt to explain in this paper.

The SANS measurements, which provide a detailed picture of the density profile, were made on low molecular weight PEO-*b*-PPO-*b*-PEO copolymers adsorbed on particles.[1,2] The brush thickness was found to scale approximately as $Z_{PEO}^{0.5}$, where Z_{PEO} is the degree of polymerization of the PEO blocks. Killmann et al. measured the hydrodynamic thickness of a PEO-*b*-PPO-*b*-PEO coated latex[3] and found a similar result: it scaled as $Z_{PEO}^{0.55}$. Surface force experiments measure the long-range force on two crossed cylinders resulting from the interacting layers on each surface. Taunton et al.[5-7] used terminally adsorbed PS chains in toluene and xylene, with five degrees of polymerization ranging from about 250 to 6000. The range of the force scaled approximately as $Z^{0.6}$ (except for the highest molecular weight case). Hadzioannou et al. used[4] PV2P-*b*-PS, in which the PV2P adsorbs and the PS extends in solution. They interpreted their results in terms of the scaling theory[10-13] (described below) and concluded[14] that for the good solvent case the range of the forced scaled *linearly* with Z_{PS}. On the other hand, Ansarifar and Luckham[8] measured force curves for three sets of PV2P-*b*-PBS copolymers in toluene and found the onset of the force scaled as $Z_{PBS}^{0.7}$. They also incorporated the data of Hadziioannou et al.[4] and concluded that both sets of measurements are consistent with this $Z^{0.7}$ dependence. Finally, Marra and Hair used high molecular weight PEO-*b*-PS copolymers.[9] When two particular cases were compared, $Z_{PS} \simeq 850$ and $Z_{PS} \simeq 2400$, the range of the force apparently scaled *faster* than linearly with Z_{PS}.

In order to qualitatively understand the full range of these results, it is useful to identify two limits, characterized in terms of the degree of polymerization of the dangling block Z_A and the average surface area per poly-

0024-9297/90/2223-3321$02.50/0

Table I
Dependence of x_{max} and ϕ_{max} on Z and Σ for Low Surface Density, $\Sigma \simeq \Sigma_C$, Expressed As $x_{max} \propto Z^a/\Sigma^b$ and $\phi_{max} \propto Z^c/\Sigma^d$ [a]

	a		b		c		d	
χ	SCF	isolated chains	SCF	isolated chains	SCF	isolated chains	SCF	isolated chains
0.4	2/3	3/5	0	0	>1/5	2/5	0.85	1
0.5	0.55	1/2	0	0	>1/3	1/2	1	1
0.6	1/3	<1/2	<0	0	>2/3	>1/2	>1	1

[a] The powers extracted from the self-consistent-field calculations are listed under the subheading "SCF". They were extracted from the numerical work for the largest values of Σ/Σ_C which we included; these values of Σ/Σ_C are listed in the captions for Figures 10–13. For the poor solvent case, the calculations are beyond the applicability of mean-field theory, and the exponents should be considered only approximate. The corresponding exponents for a collection of isolated grafted chains, where given, are listed under the subheadings "isolated chains".

Table II
Dependence of x_{max} and ϕ_{max} on Z and Σ for High Surface Density, $\Sigma \ll \Sigma_C$, Expressed As $x_{max} \propto Z^a/\Sigma^b$ and $\phi_{max} \propto Z^c/\Sigma^d$ [a]

	a		b		c		d	
χ	SCF	high MW limit	SCF	high MW limit	SCF	high MW limit	SCF	high MW limit
0.4	>4/5	1	0.3	1/3	<1/15	0	2/3	2/3
0.5	4/5		0.25		1/12		1/2	
0.6	3/5		0.4		1/8		1/4	

[a] The powers extracted from the self-consistent-field calculations are listed under the subheading "SCF". They were extracted from the numerical work for the smallest values of Σ/Σ_C which we included; these values of Σ/Σ_C are listed in the captions for Figures 10–13. The corresponding exponents for the high molecular weight limit in good solvent, treated by Alexander and de Gennes[10-13] and by Milner, Witten, and Cates,[15-18] where given, are listed under the subheadings "high MW limit". Our numerical work indicates that the limiting values of the exponents are the same for good and Θ solvents.

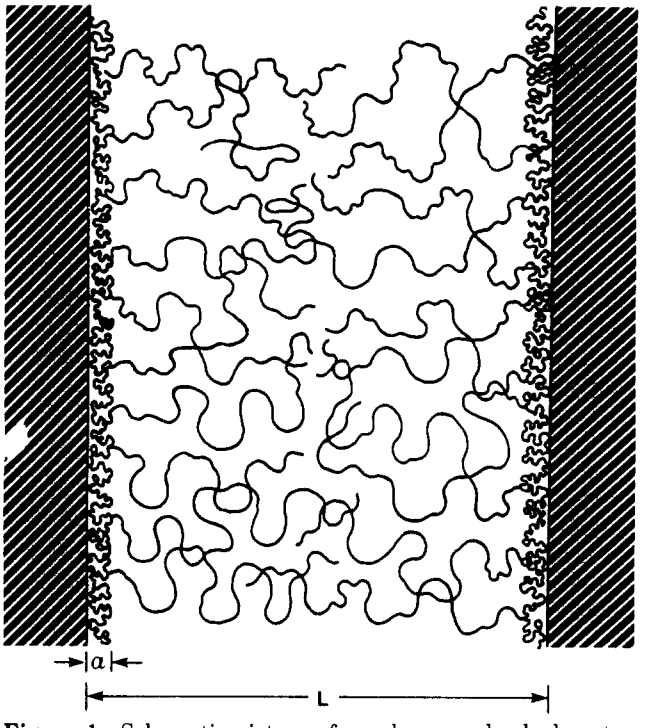

Figure 1. Schematic picture of copolymers adsorbed on two parallel surfaces separated by a distance L. One block of each copolymer, which we label the B block in the text, adsorbs tightly on a surface. The other block, which we label the A block, extends into the region between the surfaces. The copolymer joints are located in the interphases of width "a" associated with each surface.

mer, Σ. For very low coverage, i.e., small Z_A and/or large Σ, the molecules are essentially isolated chains, whereas in the opposite limit they highly interpenetrate and stretch away from the surface. The crossover between the two limits can be characterized approximately using the cross-sectional area of an isolated molecule in solution, denoted Σ_C, which corresponds approximately to a threshold for neighboring grafted molecules to overlap. To within a numerical factor, $\Sigma_C \simeq R_g^2$, where R_g is the unperturbed radius of gyration. In good and Θ solvents, $R_g \simeq Z_A^{\nu} b_A$, with b_A the Kuhn statistical length, and the values of ν are very close to $^3/_5$ and $^1/_2$, respectively.

In the limit of low coverage, the brush thickness, x_{max}, scales as an isolated molecule and so is independent of Σ

$$x_{max} \propto Z^a/\Sigma^b \tag{1.1}$$

with $a = \nu$ and $b = 0$. Also of interest is the maximum polymer volume fraction within the layer, ϕ_{max}. Because it includes an averaging parallel to the surface, it depends on the density within each molecule and on the density of grafted chains, Σ^{-1}, so

$$\phi_{max} \propto Z^c/\Sigma^d \tag{1.2}$$

with $c = 1 - \nu$ and $d = 1$. These powers are summarized in Table I.

The opposite, high-coverage limit of high Z_A and/or high graft density has been discussed by Alexander and de Gennes (hereafter referred to as AdeG)[10-13] and by Milner, Witten, and Cates (MWC).[15,16] In the scaling theory of AdeG the polymer profile, $\phi_A(x)$, is flat except for two "adjustment" regions. The first one is a depletion layer near the surface, in which the density rises from zero to the constant plateau value, and the second is a tail region in which the density falls to zero. Both these regions extend over distances comparable to the average distance between grafts, which scales as $\Sigma^{1/2}$. The layer thickness is predicted to scale *linearly* with molecular weight. It and ϕ_{max} scale as in eqs 1.1 and 1.2 but with exponents and $a = 1$, $b = ^1/_3$, $c = 0$, and $d = ^2/_3$ (at constant attachment density). These powers are included in Table II.

MWC[15,16] exploited the formal equivalence of the argument of the functional integral for the partition function with the "action" describing the classical mechanics of a particle moving in a potential and derived an analytic solution of the self-consistent equations describing the mean-field theory of the grafted polymer brush. Their solution is strictly correct in the limit of infinite molecular weight, highly stretched molecules (induced by $\Sigma \ll \Sigma_C$ in our notation) and in good solvent (requiring a positive excluded-volume parameter w). They predicted a *parabolic* profile, which decreases monotonically to zero

at x_{max} with a discontinuous derivative. (For very high coverage, they argued that $\phi_A(x)$ exhibits a plateau near the surface, followed by a parabolic decrease.) Both the depletion region near the surface and the extended tail were neglected. This is justified in this limit because as $Z_A \to \infty$ the total thickness of the layer scales linearly with Z_A, and in comparison the adjustment regions become negligible. In later work, Milner, Wang, and Witten considered formally finite molecular weight corrections,[17] and MWC included polydispersity.[18] Each of these corrections is most important at the tip of the brush.

Even though the predicted density profiles differ qualitatively, MWC predicted the same scaling laws as AdeG, but augmented by specific dependences on the excluded-volume parameter w, namely

$$x_{max} \propto w^{1/3} \qquad \phi_{max} \propto 1/w^{1/3} \tag{1.3}$$

Both models have been used to interpret the surface force measurements.[14,16,18,19] In these calculations the tails of the density distributions were ignored, and it was assumed that the two brushes retract uniformly with no interdigitation. This implies that the onset of the force occurs at a surface separation that is twice the individual brush thickness and that each compressed brush retracts linearly with surface separation.

Real systems should fall between these limits; the molecular weight and surface coverage are finite. Furthermore, in the surface force apparatus the opposing profiles both interdigitate and deform as they retract. The goals of this paper include an examination of the extent to which the idealized models for the high-coverage limit correspond to experimental conditions and to the full numerical calculations. We include calculations of the polymer profiles, the long-range forces and changes in the polymer profiles when two surfaces are brought together, covering a range of conditions. (Some of our preliminary results were presented earlier.[20]) We study both single-surface and double-surface geometries. The calculations are based on a theory of copolymer blends,[21-23] which is in turn based on the earlier work of Edwards and Dolan[24,25] and of Helfand and co-workers.[26-28] It is a mean-field self-consistent theory, involving lengthy but not unreasonable computer calculations. We have developed convergence procedures that are nearly automatic, and it is now not difficult to perform many of these calculations on modest computers. The computer code is available upon request.

Other numerical work has been reported by Cosgrove et al.,[2,29] Muthukumar and Ho,[30] and Murat and Grest.[31] In addition, these models can be used in related work; for example, Marques, Joanny, and Leibler[32,33] and Munch and Gast[34] used the step function profile similar to that of Alexander and de Gennes[10-13] in developing theories of copolymer adsorption in equilibrium with bulk. In related work, Theodorou has developed lattice models for bulk homopolymer/surface and bulk copolymer/surface systems.[35] The long-range forces between two surfaces with adsorbed copolymers have been modeled by Hadziioannou et al.,[4] Taunton et al.,[5-7] Milner et al.,[16,18] Milner,[19] Patel et al.,[14] and Muthukumar and Ho.[30]

Our use of mean-field theory limits the range of validity of the calculations.[36,37] For uniform polymer/solvent systems, the limitations can be stated formally in terms of the degree of polymerization and stiffness of the polymer, the polymer concentration, and the solvent quality as characterized by either the Flory interaction parameter (χ) or the related excluded-volume parameter. In either the dilute or semidilute regimes, mean-field theory is appropriate for polymers in a Θ solvent, which corresponds to $\chi \simeq 0.5$. In near-Θ conditions, mean field is valid if the polymer density is sufficiently large. However, in the current problem the polymer density is not uniform and, even for relatively high overall polymer content, can vary smoothly from a relatively high value to zero. Consequently, the quantitative criteria developed for uniform systems cannot be applied. We have, therefore, taken the following approach. First, we have concentrated on systems not too far from Θ conditions. Second, we have tested the calculations by making detailed comparison with experiments for good, Θ, and poor solvents. Finally, we have intentionally explored the anticipated limits of mean-field theory, including in the comparisons the good solvent case of PS/toluene.[9] In this system the degree of polymerization of the PS block is about 900, and so in a uniform system significant polymer entanglement should occur for PS volume fractions in excess of about $\phi \simeq 0.01$. The calculations indicate that in these experiments ϕ varies from a maximum, which is about 0.03, down to zero, and so one might expect the calculations to be at best qualitatively correct. However, the agreement turned out to be quite good.

The rest of the paper is origanized as follows. In section 2, we present the formalism for calculating density profiles and the resulting long-range forces. The details of the calculations are described in the Appendix. In the next two sections we present results. Section 3 considers the case when only one surface is present and contains a detailed examination of the polymer profiles, including their dependence on molecular weight, surface coverage, and solvent quantity. We go on to the case of two surfaces in section 4, including the long-range force calculation. In particular, we correlate the changes in the density profiles as the surfaces are brought together with the value of the force at each separation. We examine the interdigitation of the brushes attached to each surface, the retraction of these brushes (and extension in some regimes), changes in the profile shapes, and the details of the force curves.

We also examine the extraction of information about the profiles from the force curves, in particular, the predicted linear scaling of the brush thickness with the molecular weight of the corresponding block.[10-18] Previous interpretations of some experiments have indicated that the range of the force also scales linearly with molecular weight, and this has been taken as evidence supporting this prediction. We have concluded that this agreement is model dependent and that, even in experiments in which the range of the force *appears* to scale linearly with molecular weight, the thickness of the brush, with or without the "tail", may not. This can also explain the apparent scaling of the range of the force that is faster than linear with Z_{PS} in the experiment of Marra and Hair.[9] In the final section we summarize our conclusions. Throughout the paper, we concentrate on the physical picture of the system provided by the numerical work and on the extraction of general results such as scaling relations and the ranges of their applicability.

2. Formalism

Our model system is illustrated in Figure 1. Two infinite, flat, parallel surfaces are immersed in solvent. Attached to each surface are diblock copolymers; one block of each copolymer, labeled the B block, adsorbs tightly onto a surface, whereas the other (A block) extends into the interior region between the surfaces. There is an interfacial region at each surface in which the local volume fraction of adsorbed B-type material decreases from unity

at the surface to zero in the interior, where solvent, S, and the A-type copolymer coexist. We assume the copolymer joints are randomly distributed throughout layers of thickness "a" at each wall; we choose $a = 2b_A$, where b_A is the Kuhn statistical length for the A block polymer.

We calculate the free energy per unit area, E, as a function of surface separation, L. It is directly related to the measured force, F, by the Deryaguin approximation[38]

$$F(L)/R = 2\pi[E(L) - E_\infty] \tag{2.1}$$

where R is the geometric mean of the radii of curvature of the cylinders and E_∞ is the limiting value $E(L\to\infty)$. In practice, for this limit we take L to be large enough for there to be no overlap of polymers attached to opposite surfaces.

To calculate $E(L)$, we use a recent theory of copolymer blends in which one of the copolymer blocks is amorphous and the other is crystallizable.[39] The morphology in that case consists of alternating amorphous and semicrystalline layers, with the joints localized in interphases between the layers. Each layer can also contain compatible solvent. The picture of each amorphous layer in that system, including the two interphases at the edges, is identical with our picture of the copolymer/solvent system between the two surfaces in the present case.

For section 2 of ref 39, $E(L)$ can be written as

$$\frac{E(L)}{k_BT} = E_{int}(L) + \int_0^L dx\,[\rho_{OS}\phi_S(x)\ln\phi_S(x) - \rho_{OA}w_A(x)\phi_A(x)] - \frac{2}{\Sigma}\ln\langle q_1(Z_A)\rangle \tag{2.2}$$

The first term in eq 2.2 is the interaction energy of all components (in units of k_BT), $\phi_\kappa(x)$ is the local volume fraction of component κ at position x, $\rho_{O\kappa}$ is the density of pure component κ (monomers per unit volume), Z_A is the degree of polymerization of the A block, Σ is the average surface area per copolymer, and w_A and $\langle q_1(Z_A)\rangle$ are discussed below. We assume the system is incompressible, so that, locally

$$\phi_A(x) + \phi_B(x) + \phi_S(x) = 1 \tag{2.3}$$

everywhere between the surfaces.

The enthalpic interactions are described via generalized Flory parameters $\chi_{\kappa\kappa'}$, which are defined using the solvent for the reference density. The approximate range of the interactions is given by σ, taken to be equal for all interactions. We choose $\sigma = b_A$. E_{int} can be expressed as

$$E_{int}(L) = \rho_{OS}\int_0^L dx\,\{\chi_{SA}[\phi_S(x)\,\phi_A(x) - (\sigma^2/6)\phi'_S(x)\phi'_A(x)] + \chi_{SB}[\phi_S(x)\,\phi_B(x) - (\sigma^2/6)\phi'_S(x)\,\phi'_B(x)] + \chi_{AB}[\phi_A(x)\,\phi_B(x) - (\sigma^2/6)\phi'_A(x)\,\phi'_B(x)]\} \tag{2.4}$$

The prime on $\phi_S(x)$, etc., denotes diffraction. Written in this form, the interactions between all pairs of components can be seen.

In this paper, we do not attempt to calculate the density profile of the adsorbed block, $\phi_B(x)$. Instead, we assume that for very tightly adsorbed B blocks it is independent of surface separation (as long as the surfaces are not squeezed too tightly together). In the interphase region where A and B blocks coexist, we model it simply by

$$\phi_B(x) = 1 - \tanh^2(x/l) \tag{2.5}$$

with l chosen so that $\phi_B = 0.5$ at $x = b_A$. This choice is consistent with an interphase width characterized by $a = 2b_A$. Thus the procedure includes a nontrivial description of the A–B interphase, with at least qualitatively realistic descriptions of the profiles and interactions in the region. Any error in this profile should not significantly affect the difference $[E(L) - E_\infty]$, although it would affect $E(L)$ and E_∞ individually. On the other hand, this simple profile cannot model competing A and B adsorption.

An alternative form for $E_{int}(L)$ can be obtained by subtracting from eq 2.4 terms that depend only on $\phi_B(x)$, i.e., are independent of L, giving

$$E_{int}(L) = \rho_{OS}\int_0^L dx\,\{\chi_{SA}[\phi_S(x)\,\phi_A(x) - (\sigma^2/6)\phi'_S(x)\phi'_A(x)] + [\chi_{AB} - \chi_{SB}][\phi_A(x)\,\phi_B(x) - (\sigma^2/6)\phi'_A(x)\,\phi'_B(x)]\} \tag{2.6}$$

This shows that the effects of the surface depend on the difference $(\chi_{AB} - \chi_{SB})$ and not on χ_{AB} and χ_{SB} individually. This difference is analogous to the differential adsorption parameter, χ_S, of lattice theories of polymer adsorption.[40]

The profiles $\phi_A(x)$ and $\phi_S(x)$, as well as the other terms in $E(L)$, are calculated by solving self-consistent diffusion equations for the polymer distribution functions. Three such functions are needed, which we label $q_0(x,t)$, $q_1(x,t)$, and $q_2(x,t)$ and which satisfy

$$\frac{1}{Z_A}\frac{\partial}{\partial t}q_i(x,t) = \left[\frac{b_A^2}{6}\frac{\partial^2}{\partial x^2} - w_A(x)\right]q_i(x,t) \tag{2.7}$$

All the q_i's are subject to the same boundary conditions

$$q_i(0,t) = q_i(L,t) = 0 \tag{2.8}$$

but different initial conditions

$$q_0(x,0) = 1 \tag{2.9}$$

$$q_1(x,0) = \theta(a - x) \tag{2.10}$$

$$q_2(x,0) = \theta[x - (L - a)] \tag{2.11}$$

From the solutions of eqs 2.7–2.11 the local polymer volume fraction is constructed via

$$\phi_A(x) = \phi_{A1}(x) + \phi_{A2}(x) \tag{2.12}$$

with

$$\phi_{Ai}(x) = \frac{\bar{\phi}_A}{2Z_A\langle q_1(Z_A)\rangle}\int_0^{Z_A} q_i(x,t)\,q_0(x,Z_A-t)\,dt \tag{2.13}$$

for $i = 1$ and 2. Here $\bar{\phi}_A$ is the overall volume fraction of the A-type monomers in the region, which for a given surface area per joint, Σ, varies inversely with L,

$$\bar{\phi}_A = \frac{2Z_A}{\rho_{OA}\Sigma}\frac{1}{L} \tag{2.14}$$

and

$$\langle q_1(Z_A)\rangle = \frac{1}{L}\int_0^L q_1(x, Z_A)\,dx \tag{2.15}$$

is the average of $q_1(x,Z_A)$ over the region. This also appears in eq 2.2 for $E(L)$.

We interpret $\phi_{Ai}(x)$ as the volume fraction of polymer A at the point x due to the molecules attached to surface i. The functions $q_1(x,t)$ and $q_2(x,t)$ are proportional

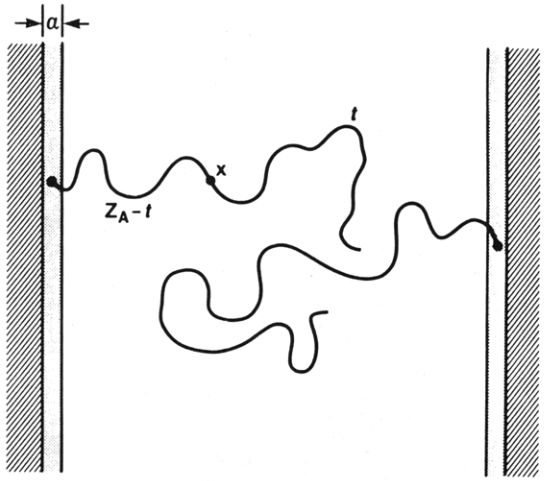

$$\phi_A(x) \propto \sum_{i=1}^{2} \int_0^{Z_A} dt\, q_i(x,t)\, q_0(x, Z_A - t)$$

Figure 2. Calculation of polymer density from the convolution of the probability functions.

to the probability that a section of the molecule of length t ends at x given that it begins somewhere in the interphase regions 1 and 2, respectively; $q_0(x,Z_A-t)$ is proportional to the probability that a section of length $Z_A - t$ ends at x given that it begins somewhere between the surfaces. The convolution, eq 2.13, is illustrated schematically in Figure 2.

To solve the diffusion equation for each q_i, the self-consistent potential $w_A(x)$ is needed. It is given by

$$w_A(x) = w_A^m + \frac{\rho_{OS}}{\rho_{OA}}\left\{\ln\left[\frac{\phi_S^m}{\phi_S(x)}\right] + (\chi_{AB} - \chi_{SB})[\phi_B(x) + (\sigma^2/6)\phi''_B(x)] + \chi_{AS}[(\phi_S(x) - \phi_S^m) - (\phi_A(x) - \phi_A^m) + (\sigma^2/6)[(\phi''_S(x) - \phi''_S{}^m) - (\phi''_A(x) - \phi''_A{}^m)]]\right\} \quad (2.16)$$

Here the superscript "m" implies the value of the function evaluated at the midpoint of the region, for example, $\phi_S^m = \phi_S(x=L/2)$. The overall level of the potential is arbitrary; w_A^m can be any convenient value. As in eq 2.6, only the difference $(\chi_{AB} - \chi_{SB})$ is significant.

The quantity $\langle q_1(Z_A)\rangle$ is related to the entropy of a chain. However, the interpretation is complicated by the fact that its value depends on w_A^m. (The value of the free energy does not, because of a corresponding dependence of the second term of eq 2.2.) If w_A^m is chosen so that

$$\int_0^L dx\, w_A(x)\, \phi_A(x) = 0 \quad (2.17)$$

then $\langle q_1(Z_A)\rangle$ is the mean-field chain entropy.

We need to know $w_A(x)$ in order to solve the diffusion equation and then calculate $\phi_A(x)$ from eqs 2.3, 2.5, and 2.7–2.15. However all the $\phi_\kappa(x)$ values are needed in order to calculate $w_A(x)$. Hence the problem must be solved self-consistently for each surface separation. Our procedure is described in Appendix A. Once a converged solution is obtained, $E(L)$ is calculated from eqs 2.2, 2.6, and 2.15.

3. Adsorbed Copolymers: Polymer Profiles at One Surface

3.1. General Results. We begin by considering polymer profiles when there is only one surface present. In the current formalism, this corresponds to $L \to \infty$. Except in subsection 3.3, all results in this section are for the case of PS blocks in a solvent whose pure-component density, ρ_{OS}, is the same as that of cyclohexane. This choice enters the calculation through the value of the Kuhn statistical length, which we take to be 0.71 nm,[41] and through the mean-field potential $w_A(x)$; for this case $\rho_{OS} = 1.1\rho_{OA}$.[41,42] Changing these parameters would have quantitative, but not qualitative, effects. In this paper we ignore any difference in surface affinity of the PS and the solvent, choosing $\chi_{AB} = \chi_{SB}$ or, in terms of the differential adsorption parameter, $\chi_S = 0$.

Figures 3–9 show polymer profiles, $\phi_A(x)$, for good, Θ, and poor solvents, low to high molecular weight, and low to high surface coverage. Not shown are the profiles of the adsorbed block, $\phi_B(x)$, decreasing from unity at the surface to zero at about 2.5 nm from the surface in accord with eq 2.5, and of the solvent, $\phi_S(x) = 1 - \phi_A(x) - \phi_B(x)$. Since in this section we are interested in the profile of only the A polymer, we simplify the notation by dropping the subscripts and denote the Flory parameter χ_{AS}

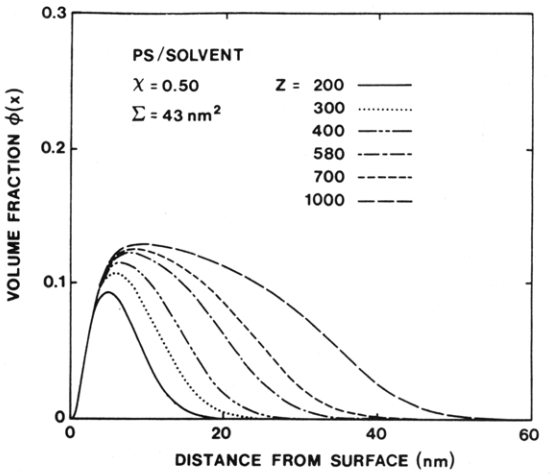

Figure 3. Polymer profiles as a function of the degree of polymerization of PS (dangling block) Z, for $\Sigma = 43$ nm^2 and $\chi = 0.5$ (near-Θ solvent). Figures 3–13 were calculated assuming that the polymer chain has Kuhn statistical length b and pure-component density ρ_{OA} corresponding to PS and that the solvent has pure-component density ρ_{OS} corresponding to cyclohexane.[41] These specific choices have quantitative but not qualitative effects. In all cases, the profiles rise from zero to a maximum which is a finite distance from the surface. This is followed by a decrease, which is initially approximately parabolic but evolves into a smooth, extended "tail".

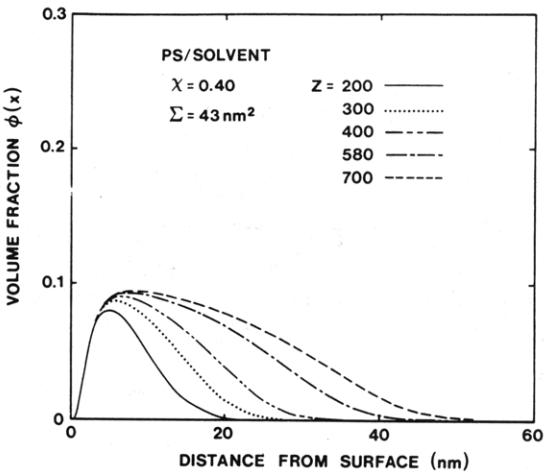

Figure 4. Polymer profiles as a function of Z for $\Sigma = 43$ nm^2 and $\chi = 0.4$ (better than Θ solvent). See the caption to Figure 3 for more details.

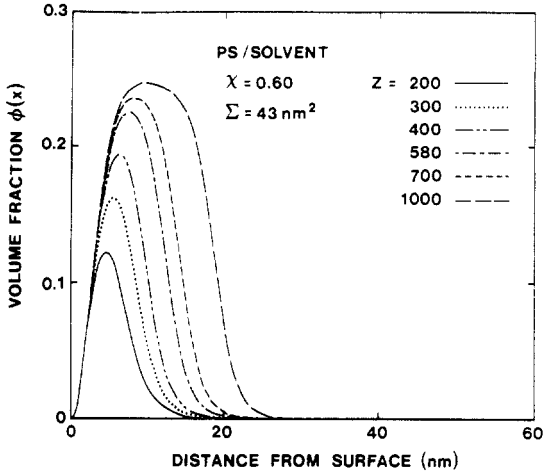

Figure 5. Polymer profiles as a function of Z for $\Sigma = 43$ nm^2 and $\chi = 0.6$ (worse than Θ solvent). See the caption to Figure 3 for more details.

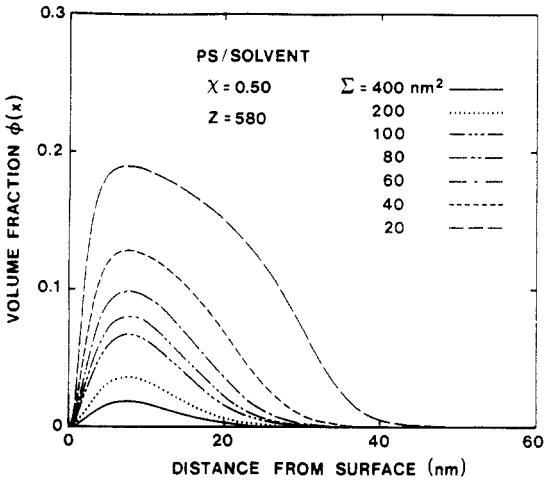

Figure 6. Polymer profiles as a function of Σ for $Z = 580$ and $\chi = 0.5$ (near-Θ solvent). See the caption to Figure 3 for more details.

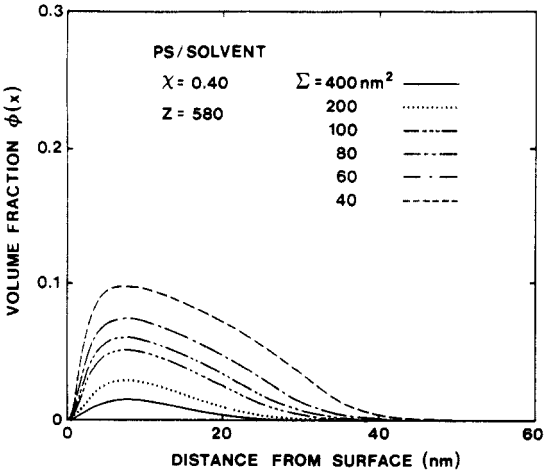

Figure 7. Polymer profiles as a function of Σ for $Z = 580$ and $\chi = 0.4$ (better than Θ solvent). See the caption to Figure 3 for more details.

simply by χ.

The most important general conclusion to be drawn from these figures is that in all cases the density profiles are qualitatively the same, rising from zero to a maximum value ϕ_{max} and then decreasing toward and eventually returning to zero in a smooth and extended "tail-like" region. The initial rise is analogous to the depletion region of the AdeG model. The decrease that follows

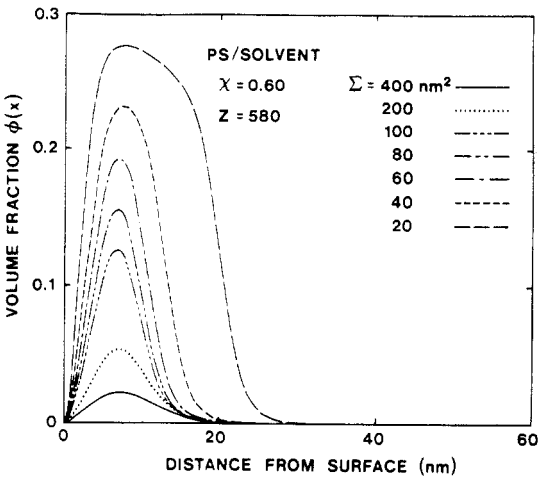

Figure 8. Polymer profiles as a function of Σ for $Z = 580$ and $\chi = 0.6$ (worse than Θ solvent). See the caption to Figure 3 for more details.

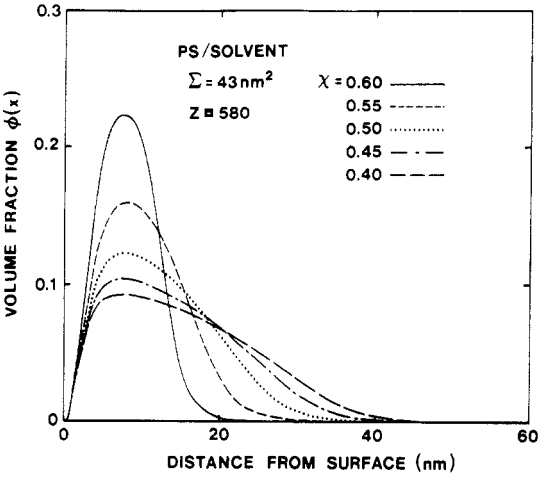

Figure 9. Polymer profiles as a function of solvent quality for $Z = 580$ and $\Sigma = 43$ nm^2. See the caption to Figure 3 for more details.

is initially at least approximately parabolic, as in the MWC model but in contrast to the step function profile of the AdeG model. However, the profiles evolve into extended tails, returning smoothly to zero with a continuous derivative.

Figures 3–5 show the effects of the degree of polymerization of the PS block for an average surface area per graft of $\Sigma = 43$ nm^2. (This is the best value for the experiments of Hadziioannou et al.,[4] which are discussed below.) Figure 3 is for the near-Θ solvent, $\chi = 0.5$. For small Z, e.g., $Z = 200$, the distribution rises from zero at the surface to ϕ_{max} at $x \simeq 5$ nm and then immediately begins to decrease, tailing off to zero at $x \simeq 20$ nm. As Z is increased, both ϕ_{max} and its distance from the surface increase by small amounts. The maximum broadens, and the tail extends farther out.

Figure 4 shows similar results but for a good solvent, with $\chi = 0.4$. (We were unable to obtain a converged self-consistent solution for $Z = 1000$ for these values of χ and Σ.) The profiles are similar to those of Figure 3 but differ quantitatively in two ways. First, for a given Z (and Σ), the spatial extent of the profile is increased, and ϕ_{max} is correspondingly decreased. Second, there is less variation in the value and location of ϕ_{max} with Z.

Figure 5 illustrates results for a poor solvent, with $\chi = 0.6$. For the small values of Z, the profiles are similar to those of Figures 3 and 4, except that the spatial extent of each profile is reduced and ϕ_{max} is correspondingly

increased. For large Z, a small plateaulike region is beginning to form. The value and location of ϕ_{max} vary more than for the case $\chi = 0.5$.

Figures 6–8 illustrate the effects of varying the graft density (Σ^{-1}) for the case $Z = 580$. (This corresponds to PS blocks used in experiments of Hadziioannou et al.[4]) In Figure 6, for which $\chi = 0.5$, for large Σ the profile is low and very broad, with a tail that extends over nearly the entire profile. As the surface density increases (Σ decreases), ϕ_{max} increases, but its location remains nearly constant. This differs from the variation of the size of the depletion layer predicted by AdeG. The maximum extent appears to be nearly independent of Σ for $\Sigma \gtrsim 100$ nm^2 but begins to increase as Σ is reduced below about 80 nm^2. Comparing Figures 3 and 6 shows that the effects of increasing Z are qualitatively similar to those of decreasing Σ. This is not surprising, since the interpenetration of neighboring molecules is characterized by the ratio Σ_C/Σ, which is proportional to Z/Σ.

The corresponding profiles in good solvent, $\chi = 0.4$, are shown in Figure 7. For each value of Σ, the profiles are more extended than those in the Θ solvent, consistent with Figures 3 and 4. As was the case when $\chi = 0.5$, ϕ_{max} increases as Σ decreases, but its location is nearly constant. In contrast to the Θ solvent, in this case the maximum spatial extent depends on Σ for all the values of Σ. Finally, decreasing Σ has a similar effect as increasing Z, as for the Θ solvent case.

The corresponding profiles in worse than Θ solvent, $\chi = 0.6$, are shown in Figure 8. They are of course higher and less extended than the two previous cases, and again ϕ_{max} increases as Σ decreases. Note that in this case the spatial extent does not begin to increase with decreasing Σ until $\Sigma < 60$ nm^2. Again, decreasing Σ and increasing Z have similar effects, including inducing a small plateau region.

Finally, Figure 9 highlights the variation of the profiles with solvent quality for $Z = 580$ and $\Sigma = 43$ nm^2. (The three profiles corresponding to $\chi = 0.5$, 0.4, and 0.6 are the same as those in Figures 3–5.) There is a large change from the relatively compact profile in the bad solvent through to the extended profile in the good solvent. In all cases, ϕ_{max} is about 8 nm from the surface, and the tail region extends over a significant range.

Muthukumar and Ho[30] have performed similar self-consistent-field calculations. In their work the effective interaction was described by the excluded-volume parameter rather than the more complete description as in eq 2.16. Also, rather than using specific material parameters, i.e., the Kuhn statistical length and reference densities ρ_{Ox}, they took the polymer monomer and solvent molecule volumes to be equal. This precludes quantitative comparison with specific experiments. However, they did include a van der Waals interaction with the surfaces. For the cases that they considered, the number of eigenfunctions that they used in their expansions was much less than we needed when we considered large degrees of polymerization and surface separations. They also discretized space using a coarser grid than we found was necessary to achieve sufficient precision in the tails of the profiles.

Their calculated profiles agree qualitatively with ours. The density rises from zero at the surface to a maximum and then returns to zero over a distance that depends on the degree of polymerization, surface coverage, and solvent quality. Relative to Θ conditions, the positive excluded-volume interaction broadens and lowers the profiles, whereas in a worse than Θ solvent the profile sharpens.

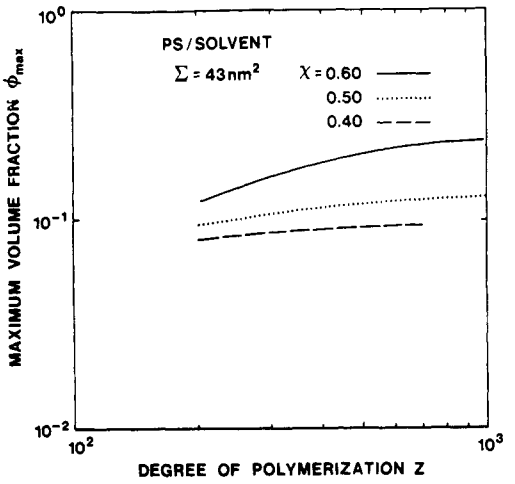

Figure 10. Value of the maximum in the polymer density, ϕ_{max}, as a function of Z for $\Sigma = 43$ nm^2 and different solvent qualities, $\chi = 0.4$, 0.5, and 0.6. The values are the peak values in Figures 3–5. In the calculations for this figure, the ratio Σ/Σ_C varies approximately from 0.03 (high Z) to 0.15 (low Z) for good solvent, from 0.1 to 0.5 for Θ solvent, and from >0.1 to >0.5 for poor solvent. See the caption to Figure 3 for more details.

The profiles also depend sensitively on surface affinity, an effect that is beyond the scope of the current paper.

Cosgrove et al.[2,29] performed self-consistent-field theory and Monte Carlo calculations for these systems. Like Muthukumar and Ho,[30] they considered the effects of surface affinity, along with solvent quality, surface coverage, and molecular weight. Their calculated density profiles are qualitatively very similar to ours except that the maximum in each profile occurs much closer to the surface. For their self-consistent calculations, they extended the lattice model developed by Scheutjens, Fleer, and co-workers in their extensive work on polymer adsorption.[37,40,43] The polymer distribution functions were obtained by inverting a large matrix, the size of which is determined by the number of lattice spacings between the two surfaces. The effective Kuhn length and the monomer volume ρ_{OA} are directly coupled to the lattice constant and hence are not independently taken from experiment. The results depend quantitatively on the lattice used, in particular, near the surface.

Finally, Murat and Grest[31] have recently published a molecular dynamics study of the two-surface geometry, for grafted chains with $Z = 50$ and 100. These are shorter than any of the chains used in this paper. They used a bend and spring model of the polymers, with monomers interacting via a shifted short-range Lennard-Jones potential, which is purely repulsive. Thus the simulations are for the good solvent regime. However, as in the work of Muthukumar and Ho[30] and Cosgrove et al.,[2,29] full quantitative modeling of specific polymer/solvent systems is not done. Qualitatively, their calculated profiles are similar to ours. The density rises from zero at the surface to a maximum and then decreases as a quasi-parabola, evolving into a tail.

3.2. Quantitative Analysis. In this section we analyze our numerical results and compare with the scaling results presented earlier for the two limits. We focus on three characterizations of the polymer profiles: the maximum volume fraction, ϕ_{max}, and two measures of the layer thickness.

Consider first ϕ_{max}. Figures 10 and 11, which are constructed from the profiles of Figures 3–8, show the increase in ϕ_{max} with increasing Z, decreasing Σ, and increasing χ. In order to make contact between these results and the earlier work on the limiting cases, we express our

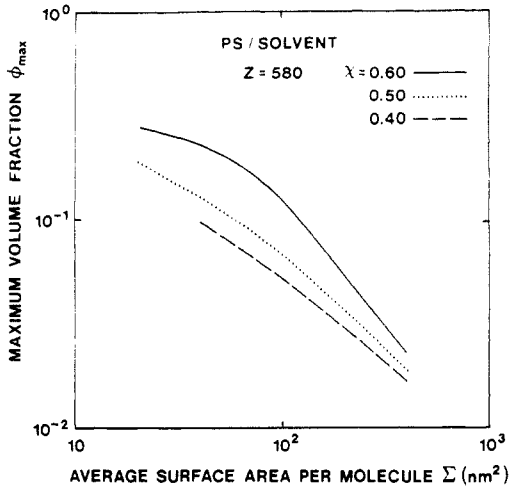

Figure 11. Value of the maximum in the polymer density, ϕ_{max}, as a function of Σ for $Z = 580$ and different solvent qualities, $\chi = 0.4$, 0.5, and 0.6. The values are the peak values in Figures 6–8. In these calculations Σ/Σ_C varies approximately from 0.04 (low Σ) to 0.5 (high Σ) for good solvent, from 0.1 to 1 for Θ solvent, and from >0.1 to >1 for poor solvent. See the caption to Figure 3 for more details.

results as power laws as in eqs 1.1 and 1.2 but note that this is only approximately correct and that powers extracted in this way are expected to vary over the range of the parameters. We include in Tables I and II the values of the exponents we find at the highest and lowest coverage that we have investigated, for direct comparison with the predicted values. The limiting values of Σ/Σ_C used in the calculations are included in the captions to Figures 10 and 11.

To interpret the results, we first identify the "threshold" surface coverage for each solvent quality. In Figure 10, for which $\Sigma = 43$ nm^2, $\Sigma_C = \Sigma$ at $Z \simeq 50$ in good solvent, $Z \simeq 100$ in Θ solvent, and $Z > 100$ in the bad solvent. Since $Z \geq 200$ for all calculations shown in Figure 10, they are all for $\Sigma < \Sigma_C$, except perhaps for some calculations for the case $\chi = 0.6$. In Figure 11, for which $Z = 580$, we have $\Sigma_C \simeq 1000$ nm^2 for a good solvent, $\Sigma_C \simeq 300$ nm^2 for a Θ solvent, and $\Sigma_C < 300$ nm^2 for a poor solvent. Since the calculations include values of Σ as high as 400 nm^2, for the poor solvent case in particular we are clearly extending into the regime $\Sigma \simeq \Sigma_C$. We do so because of an interesting qualitative effect that emerges.

Turning to the results, the variation of ϕ_{max} with Z, shown explicitly in Figure 10, depends quantitatively on the value of χ but is in all cases relatively weak. Specifically, for $\chi = 0.6$, as Z is increased by a factor of 5, ϕ_{max} increases by about a factor of 2. For the Θ solvent, the increase is about 50%, and for $\chi = 0.4$, it is only about 20%.

In terms of the approximate power law dependence, the exponent "c" in eq 1.2 ranges from about $^2/_3$ for small Z to $^1/_8$ for large Z for the case $\chi = 0.6$, from about $^1/_3$ to $^1/_{12}$ for the Θ solvent, and from about $^1/_5$ to less than $^1/_{15}$ in the good solvent. At both the highest and lowest degrees of polymerization for which we have results, these powers are still changing, apparently approaching the limiting values. However, ϕ_{max} has not yet saturated even for $Z > 700$, although it has nearly done so for the good solvent case.

The dependence of ϕ_{max} on Σ is shown in Figure 11. For the bad solvent, the inverse power, "d" in eq 1.2, is about $^5/_4$ for large Σ, but for $\Sigma < 100$ nm^2 the dependence weakens, with $d \simeq {}^1/_4$ at $\Sigma = 20$ nm^2. As noted above, in the vicinity of $\Sigma \simeq 300$ nm^2, the quantitative results should not be considered reliable. In the Θ solvent, the power varies from about unity at large Σ to about $^1/_2$ at small Σ, and for the good solvent, it varies from about 0.85 to $^2/_3$. The specific values depend quantitatively on the choice of $Z = 580$, but the trends indicated are more general. Comparing these with the expected limits, for the good solvent case our value of $d \simeq {}^2/_3$ at small Σ agrees with the AdeG and MWC models and our value of $d = 0.85$ at the largest Σ is approaching the isolated chain value of unity. For the Θ solvent, at each value of Σ the exponent "d" is slightly less that it is for the same Σ in the good solvent. Because we were able to obtain solutions to smaller Σ for the Θ solvent, we were able to push the calculation to a regime of even weaker dependence, reaching $d = 0.5$ at $\Sigma = 20$ nm^2. For the bad solvent case, we have a particularly interesting result: at large Σ the power is greater than unity. This is discussed below in conjunction with the brush thickness.

Finally, from the figures in this section it is readily seen that as χ is increased from 0.4 to 0.6 ϕ_{max} increases by as much as a factor of about 4. This dependence on solvent agrees qualitatively with the predictions of MWC. However, we found no simple exponential or power law dependence of ϕ_{max} on χ. Recalling the prediction of MWC for the good solvent case, eq 1.3, we also looked for a simple dependence on the excluded-volume parameter, which in our case corresponds to

$$w = \frac{\rho_{OS}}{\rho_{OA}}(1 - 2\chi) \tag{3.1}$$

We found no simple functional dependence of ϕ_{max} on w, power law, or exponential. In particular, for the two good solvent cases, $\chi = 0.45$ and 0.4, our calculated ϕ_{max} varied much more slowly with w than is implied by $w^{1/3}$. (The $w^{1/3}$ scaling may still apply for very good solvents at high molecular weight.)

Turning next to the thickness of the brush, we characterize it by the root-mean-squared thickness, $\langle x^2 \rangle^{1/2}$, and by its total thickness, x_{max}. The two characterizations emphasize different parts of the profiles. Because the density vanishes continuously, an operational definition of x_{max} must be chosen; we define it to be the distance from the surface such that the region $[0,x_{max}]$ contains 99% of the profile. It is worth noting that this interval does not include all of the tail. For example, for the specific case $\chi = 0.5$, $Z = 580$, and $\Sigma = 43$ nm^2, $x_{max} = 30.5$ nm. By comparison, when the related quantity x'_{max} is defined as the distance such that 99.9% of the profile is included, then in this case $x'_{max} = 36.8$ nm. This rather small fraction of the entire profile (0.9%) extends over a distance of 6 nm. On the scale in Figure 3, the profile is actually visible out to about 34 nm.

Our calculated values are shown in Figures 12 and 13. From Figure 12 we see that they both increase with increasing Z, again approximately as power laws. In the worse than Θ solvent, x_{max} varies slightly more slowly with Z than does $\langle x^2 \rangle^{1/2}$. However, in the other two solvents the two characterizations scale approximately together. This implies that the main body of the profile scales in much the same way as does the total profile (to the extent that x_{max} includes the tail.) In the following discussion we need not distinguish between them.

For $\Sigma = 43$ nm^2, in the worse than Θ solvent the scaling with Z, i.e., the power "a" in eq 3.9, varies from about $^1/_3$ for small Z to about $^3/_5$ at large Z; in the Θ solvent it varies from about 0.55 to $^4/_5$, and in the better than Θ solvent, from about $^2/_3$ to just over $^4/_5$. Once again, for the Θ and better than Θ solvents, the powers are *tending*

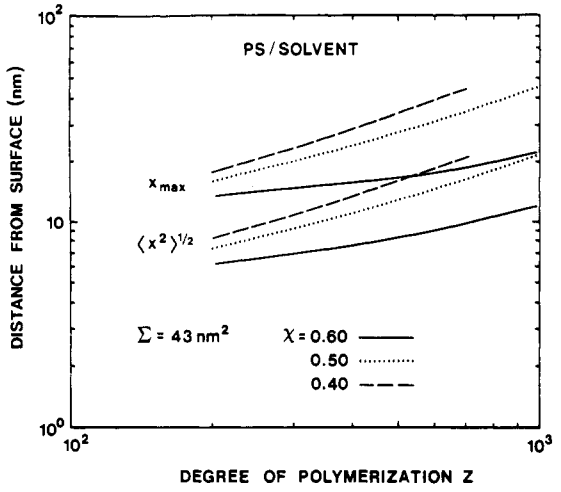

Figure 12. Root-mean-squared layer thickness, $\langle x^2 \rangle^{1/2}$, and maximum extent of the profile as characterized by x_{max}, as a function of Z for $\Sigma = 43$ nm^2 and $\chi = 0.4$, 0.5, and 0.6. In these calculations Σ/Σ_C varies over the same ranges as in Figure 10. See the caption to Figure 3 for more details.

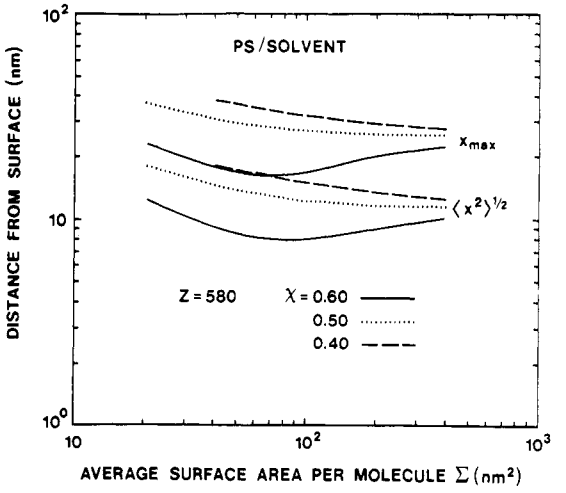

Figure 13. Root-mean-squared layer thickness, $\langle x^2 \rangle^{1/2}$, and maximum extent of the profile as characterized by x_{max}, as a function of Σ for $Z = 580$ and $\chi = 0.4$, 0.5, and 0.6. In these calculations Σ/Σ_C varies over the same ranges as in Figure 11. See the caption to Figure 3 for more details.

toward the limits of ν at small Z and unity at large Z.

Figure 13 shows the variation with Σ for the case $Z = 580$. For the good and Θ solvents, the results are as would be expected. At large Σ, the thickness is nearly independent of Σ, so the corresponding power, "b" in eq 3.9, is nearly zero. However, below $\Sigma \simeq \Sigma_C$ the chains begin to stretch away from the surface. For the good solvent case, we obtain the value $b = 0.3$ at $\Sigma = 40$ nm^2, very close to the limiting value of $^1/_3$. For the Θ solvent, at each value of Σ the scaling is slightly weaker with the power reaching $b = 0.25$ at $\Sigma = 20$ nm^2.

For the worse than Θ solvent, a qualitatively different result emerges, namely that, for certain large values of Σ, the thickness is an *increasing* function of Σ. This variation can be understood physically as follows. For very large Σ, the isolated chains are independent of one another. In a good solvent, as the graft density increases and neighboring chains begin to encounter one another, they begin to stretch away from the surface because of the favorable polymer/solvent interactions. However, in a poor solvent the opposite occurs; because of the unfavorable interactions it is initially advantageous for the chains to retract toward the surface. As Σ is further reduced, the chains continue to retract until the crowding begins to dominate, and they begin to stretch out again. The net effect is a nonmonotonic dependence of the layer thickness on Σ, as indicated in Figure 13.

We noted above that, in the poor solvent, $\phi_{max} \simeq \Sigma^{-d}$ with $d > 1$ for certain large values of Σ. This is due to this same effect. If the individual chain profiles were independent of surface coverage, then as the number of chains per unit area is increased, ϕ_{max} would scale as Σ^{-1}. However, since in this case the individual chains begin to contract toward the surface, the maximum polymer density associated each chain increases. This leads to this stronger dependence of ϕ_{max} on Σ.

Finally, Figure 13 also illustrates the increase in layer thickness with improving solvent quality for $Z = 580$ and for Σ ranging from 40 nm^2 to 400 nm^2. As was the case for ϕ_{max}, we found no simple functional dependence of either $\langle x^2 \rangle^{1/2}$ or x_{max} on either χ or the excluded-volume parameter w.

For good and Θ solvents and in the limit of high molecular weight, our density profiles would approach the parabolas predicted by MWC. In this limit the two "adjustment" regions become negligible compared with the rest of the parabolic profile. However, in each case that we have considered, the length of the tail is significant; for example, in the case considered explicitly above, about 1% of the total layer is contained in the last ≃20% of the profile extent. Furthermore, even the quasi-parabolic part of the profiles (i.e., without the tails) scales more slowly than as predicted by AdeG and MWC. Instead, its dependence varies from approximately $\langle x^2 \rangle^{1/2} \propto Z^{\nu}$ in the low-coverage regime toward $\langle x^2 \rangle^{1/2} \propto Z$ in the high-coverage regime.

3.3. Experimental Comparison. We end this section by discussing the experiments on polymer profiles at single surfaces, mentioned in the Introduction. In the SANS study of triblock PEO-*b*-PPO-*b*-PEO copolymers adsorbed on PS latex in water, the PPO adsorbs, and the two end blocks extend into solution.[1] Two samples were used, in each of which the degree of polymerization of the central block was 56, whereas the end PEO blocks had degrees of polymerization of 32 and 140, respectively. In each case the profiles had extended tails, similar to what we predict. The higher molecular weight PEO blocks extended about twice as far into the water as the lower molecular weight blocks. Since the ratio of the molecular weights is 140/32 ≃ 4.5, this corresponds roughly to an effective scaling, folding in variations in Σ, of $x_{max} \propto Z_{PEO}^{1/2}$.

We can understand this scaling on the basis of the current work (assuming that any competing adsorption of PEO does not play a significant role). From the published density profiles, we estimate that the average surface area per dangling block is $\Sigma \simeq 2$ nm^2 for the $Z_{PEO} = 32$ case and $\Sigma \simeq 6$ nm^2 for the other one. Since this is a better than Θ solvent with $\chi = 0.45$,[41] the scaling exponent for the isolated chain, ν, should be between $^1/_2$ and $^3/_5$, leading to the conclusion that $\Sigma/\Sigma_C \simeq 1$ for both cases. This is the low-coverage regime, in which the brush thickness should scale approximately as $[Z_{PEO}]^a/\Sigma^b$ with $a \gtrsim \nu$ and $b \gtrsim 0$, (see Figures 17 and 18 and Table I). Together, these imply an effective scaling of $x_{max} \propto [Z_{PEO}]^{a'}$, with $a' \lesssim \nu$, which agrees with the experiments.

As a check of this physical picture, we have performed self-consistent calculations for these cases, choosing values for Σ, Z_{PEO}, and χ as above and with the appropriate monomer volumes for PEO and water.[41] Although these should not be considered quantitatively reliable in this low-coverage regime, the calculated values of $\langle x^2 \rangle^{1/2}$,

x_{max}, and x'_{max} for the higher molecular weight case are all larger by a factor of 2.20 ± 0.05 than they are for the lower molecular weight case. This corresponds to an effective scaling exponent of $a' \simeq 0.53$, in reasonable agreement with the experiments and consistent with the above picture.

Finally, we note again that Killmann et al.[3] measured the hydrodynamic thickness of a PEO-*b*-PPO-*b*-PEO coated latex, finding it to scale as $Z_{PEO}^{0.55}$, consistent with the results of Cosgrove et al.,[1] and much slower than linear scaling.

4. Long-Range Forces between Surfaces with Adsorbed Copolymers

4.1. Introduction. In this section we calculate and analyze the long-range forces both for model systems and for systems that have been studied experimentally in the Israelachvili surface force apparatus.

Hadziioannou et al.[4] measured forces for a system of PV2P-*b*-PS and cyclohexane. Cyclohexane is a poor solvent for PV2P, which adsorbs onto the mica surface, whereas the PS extends in solution. To interpret these measurements, Patel et al.[14] modeled the PS using the AdeG scaling theory but ignored the outer tail region. Since the range of the force, which we label L_{max}, is twice the thickness of a single layer, it scales as $L_{max} \propto x_{max} \propto Z/\Sigma^{1/3}$. They further assumed that, as the surfaces are brought together, the polymer brushes retract uniformly with no interdigitation. This implies that all characterizations of the thickness of the profile, e.g., both $\langle x^2 \rangle^{1/2}$ and x_{max} in our notation, decrease linearly with surface separation, L. The force was calculated from the changes in the osmotic pressure and the elastic free energy of the compressed brushes. There are two undetermined constants, associated with the contributions of these terms.

MWC performed a similar calculation using the parabolic profiles.[16,18,19] As in the above work, they ignored the tails of the profiles and interdigitation, requiring that the layers retract uniformly as a linear function of L, which in turn implies that the polymer density midway between the two surfaces remains equal to zero. Again, the range of the force scales as $L_{max} \propto Z/\Sigma^{1/3}$. However, the parabolic profile is softer than the step function, which leads to a softer force curve. They later included polydispersity effects but still ignored the tails in the profiles and interdigitation.[18,19]

Both these models refer to the high molecular weight, high surface coverage limits in good solvent. In the rest of this section, we first present a series of force curves which we have calculated for the model system used in section 3 over a range of Z, Σ, and χ. We then calculate the force curves for good, Θ, and slightly bad solvent systems which have been studied experimentally. We compare the quantitative theoretical and experimental results, looking at the magnitude of the force at each separation, the scaling of L_{max} with molecular weight and Σ, and the detailed shape of the force curves. We go on to study the interdigitation and deformation of the profiles as the surfaces are brought together and relate these changes to the forces at each separation. In particular, we examine the relationship between the measured range of the force and the thickness of the brush.

We end here by noting that Muthukumar and Ho[30] and Murat and Grest[31] also calculated model force curves, finding results, including interdigitation, qualitatively similar to ours.

4.2. Model Calculations. In this section we calculate force curves for the model system used in section 3. The grafted polymer chain corresponds to PS and the pure-component density is that of cyclohexane; as before, this choice affects the results quantitatively but not qualitatively.

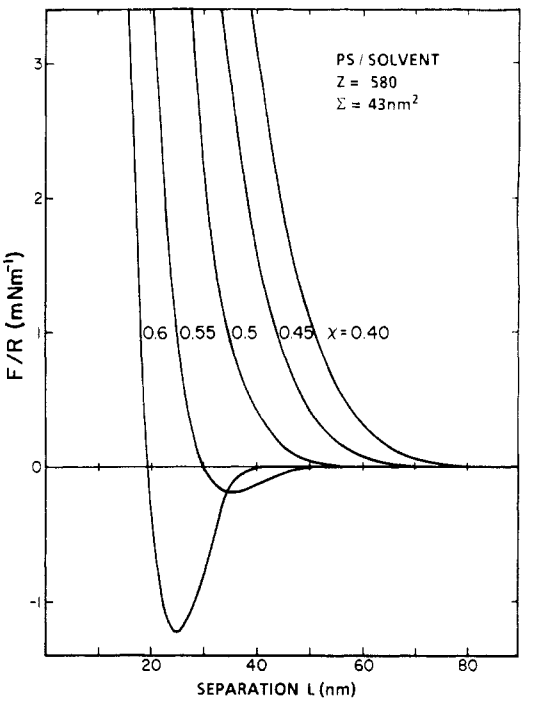

Figure 14. Calculated long-range forces, F/R, for the model system with $Z = 580$ and $\Sigma = 43$ nm^2 for different solvent qualities. In Figures 14–17, the polymer chain has Kuhn statistical length b and pure-component density ρ_{OA} corresponding to PS, and the solvent has pure-component density ρ_{OS} corresponding to cyclohexane.[41]

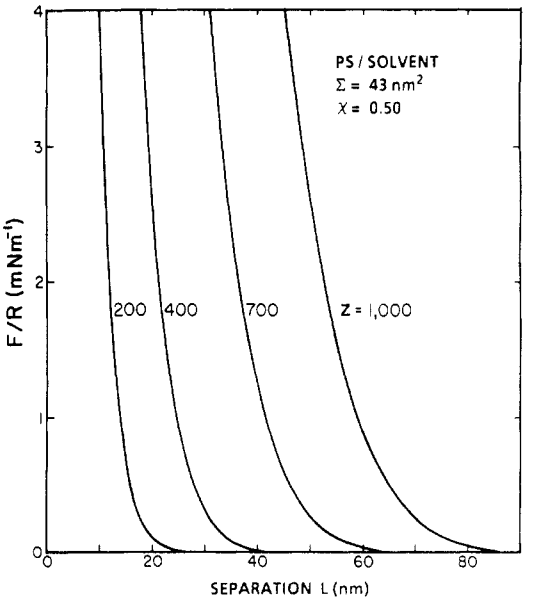

Figure 15. Calculated long-range forces, F/R, for the model system with $\Sigma = 43$ nm^2 and $\chi = 0.5$ for different values of Z. See the caption to Figure 14 for more details.

Figures 14–17 show the calculated F/R as a function of surface separation for this system. Figure 14 is for $Z = 580$ and $\Sigma = 43$ nm^2 as the experiments of Hadziioannou et al.[4] but for values of χ ranging from 0.4 to 0.6, as in section 3. Note first, Figure 14, that for $\chi \leq 0.5$ the force is everywhere repulsive, whereas for larger χ an attractive region develops; for this choice of Z, it appears for $\chi > 0.52$. As χ is increased beyond 0.52, the minimum in the force deepens and moves inward, and the repulsive part of the force becomes steeper. Over the full range

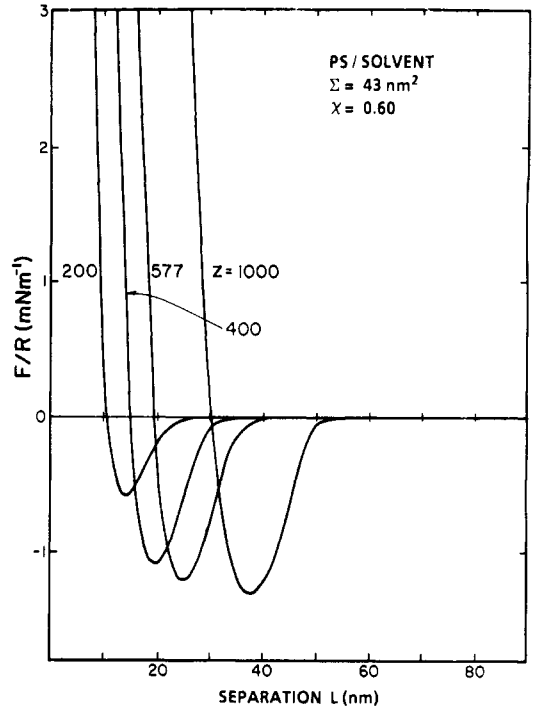

Figure 16. Calculated long-range forces, F/R, for the model system with $\Sigma = 43$ nm^2 and $\chi = 0.6$ for different Z. See the caption to Figure 14 for more details.

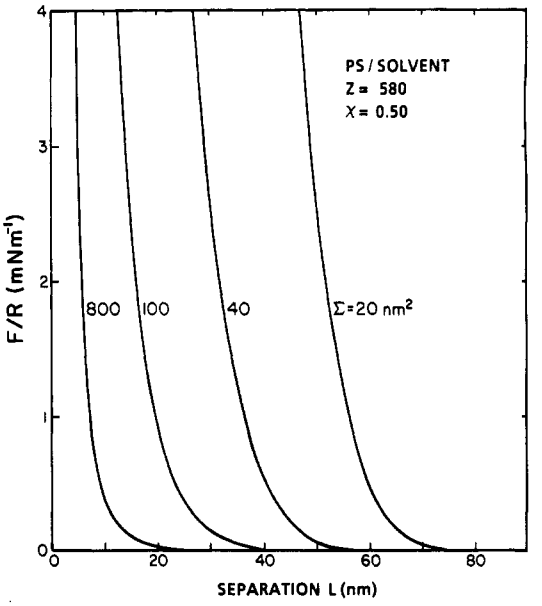

Figure 17. Calculated long-range forces, F/R, for the model system with $Z = 580$ and $\chi = 0.5$ for different Σ. See the caption to Figure 14 for more details.

of χ, L_{max} decreases for progressively worse solvents.

Figures 15 and 16 show the effects of varying Z for both near-Θ and worse than Θ solvents. In each case, the range of the force increases with increasing Z. For the case $\chi = 0.5$, Figure 15, the force curve steepens as Z is decreased. In the poor solvent, Figure 16, the shape of the repulsive part of the curve is qualitatively unchanged, but the depth and location of the minimum increase with increasing Z.

Finally, in Figure 17 we see the effects of changing the surface coverage, Σ^{-1}, for the case $Z = 580$ and $\chi = 0.5$. The main effect is to increase the range of the force; the shape is qualitatively unaltered, except that it becomes less steep as Σ is increased.

4.3. Experimental Comparison. In this section we

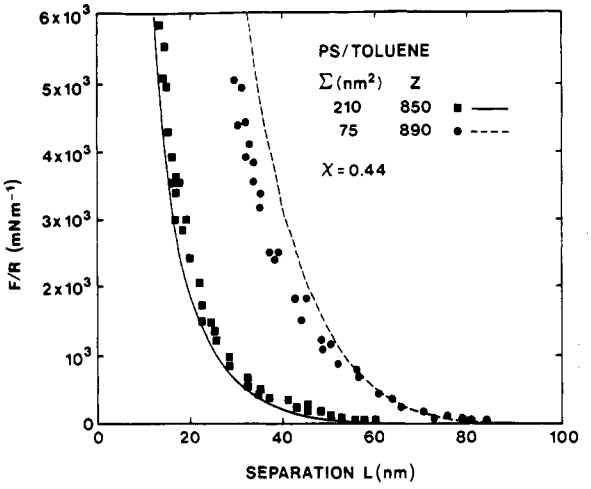

Figure 18. Long-range forces, F/R, for adsorbed PEO-b-PS in toluene, which is a good solvent for the PS. The lines are parameter-free calculations, and the points are the experimental values of Marra and Hair.[9] Values for Z and Σ are taken from the experiments; standard values were used for χ, the Kuhn statistical length b, and pure-component densities ρ_{OS} and ρ_{OA}.[41,42]

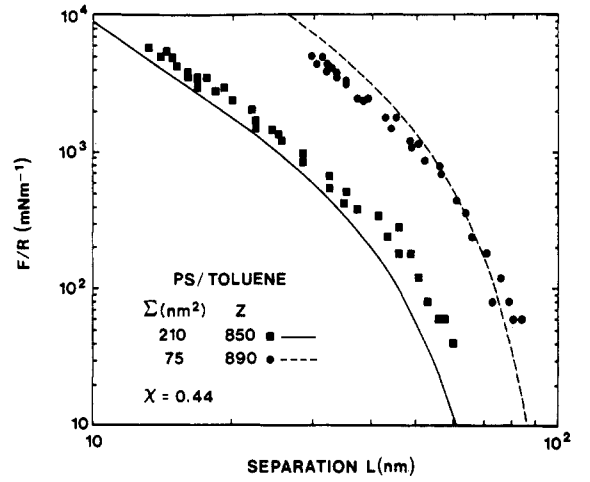

Figure 19. Long-range force, F/R, for adsorbed PEO-b-PS in toluene, the same as Figure 18 but replotted on a log–log plot. The lines are the calculations, and the points are the experimental values of Marra and Hair.[9]

choose the values of Z, Σ, PS Kuhn length $b = 0.71$ nm, and reference densities ρ_{OS} and ρ_{OA} to correspond to the experiments.[41,42] Thus this comparison provides a parameter-free test of the theory, including the use of the mean-field approximation.

We focus on two sets of experiments, summarized in Figures 18–22. The first set is for good solvent conditions, and the second is for Θ and slightly worse than Θ solvents. In these figures, the curves are the theoretical results, and the experimental results are indicated by points. At the end of this section, we make brief comparisons with other measured force curves.

For good solvent conditions, we use the experiments of Marra and Hair, which are for PEO-b-PS in toluene at room temperature.[9] Toluene is a bad solvent for PEO and a good solvent for PS, and hence the PEO adsorbs onto the surfaces. Three sets of copolymers were used; we make detailed comparisons for the two lower molecular weight sets and discuss the other set at the end of section 4.4 after we have discussed general scaling results. In the first set, the molecular weights of the blocks were 18 000 for the PEO and 90 000 for the PS; in the second, they were 8000 for the PEO and 92 000 for the PS. These experiments thus probed most directly effects of varying

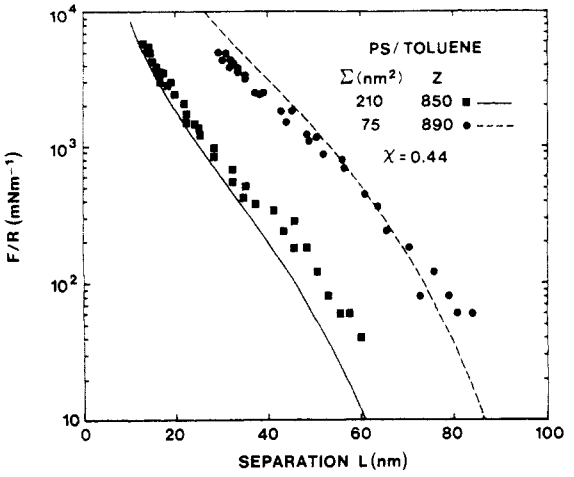

Figure 20. Long-range force, F/R, for adsorbed PEO-*b*-PS in toluene, the same as Figures 18 and 19 but replotted on a semilog plot. The lines are the calculations, and the points are the experimental values of Marra and Hair.[9]

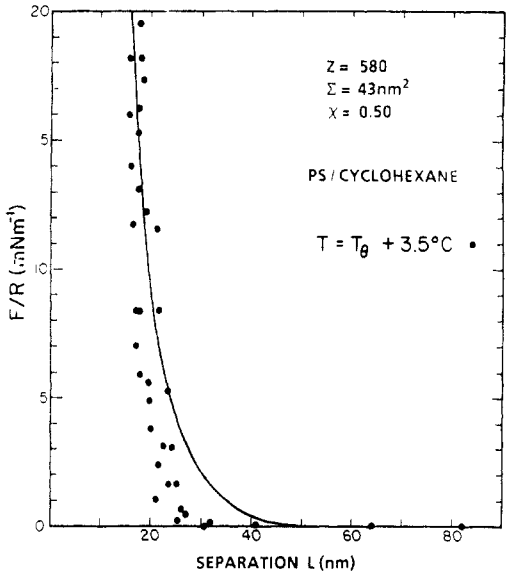

Figure 21. Long-range force, F/R, for adsorbed PV2P-*b*-PS in cyclohexane just above T_θ. The lines are the calculations, and the points are the experimental values of Hadziioannou et al.[4] Values for Z and Σ are taken from the experiments; standard values were used for χ, the Kuhn length b, and pure-component densities ρ_{OS} and ρ_{OA}.[41,42]

surface coverage, in the good solvent system.

In making quantitative comparison with experiment, four quantities are needed. The first two are the molecular weight of the PS block and the related polydispersity. The above molecular weights correspond to number average degrees of polymerization of $Z_{PS} = 850$ for the 18/90 sample and $Z_{PS} = 890$ for the 8/92 sample. The polydispersity ratio was estimated to be $\bar{M}_W/\bar{M}_N = 1.4$. In our calculations we have used these values for Z and ignored polydispersity. Next, the measured coverages correspond to $\Sigma = 210 \pm 40$ nm² for the 18/90 sample and $\Sigma = 75 \pm 15$ nm² for the other. Finally, we use $\chi = 0.44$.[41]

There is an additional effect that we have not included, which is the variation of χ with polymer volume fraction. This could be incorporated in two ways. First, as the surface separation changes, the average polymer volume fraction between the surfaces changes. Second, for a given surface separation the polymer density is nonuniform. We could obtain arbitrarily good agreement with experiment if we chose to fit χ but then would not have

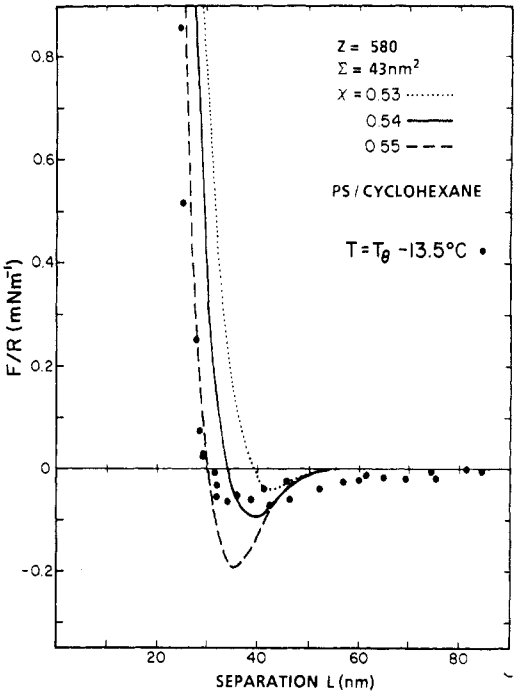

Figure 22. Long-range force, F/R, for adsorbed PV2P-*b*-PS in cyclohexane below T_θ. The lines are the calculations, and the points are the experimental values of Hadziioannou et al.[4] Values for Z and Σ are taken from the experiments; standard values were used for χ, the Kuhn length b, and pure-component densities ρ_{OS} and ρ_{OA}.[41,42]

an independent test of the theory. We also feel that it would be unwarranted given the uncertainty in the other experimental parameters, in particular Σ. Instead, we decided to use the simplest physical picture of the system, i.e., ignore polydispersity and possible variations in χ, as the test of the calculations.

Our results are shown first in Figure 18. Given that there are no fitted parameters in the calculations, we consider the overall agreement with experiment to be rather satisfying over the full range of L, in particular for the 18/90 sample.

As a further test of the calculations, we have replotted the data of Figure 18 twice, first in Figure 19 as a log–log plot and then in Figure 20 as a semilog plot. These figures indicate that for the 18/90 sample our calculations underestimate the range of the force by about 10 nm. There are at least two possible sources of this discrepancy, the first of which is polydispersity. As noted earlier, MWC[18,19] included this in their model, finding the largest corrections to the force to occur at large separation; i.e., $L \simeq L_{max}$. The polydisperse brush is predicted to be thicker than the monodisperse brush by a factor of order $(\bar{M}_W/\bar{M}_N - 1)^{1/2}$, which is more than enough to account for the current discrepancy. Alternatively, we note that at these separations the force is due largely to the interpenetrating tails of the opposing profiles, and as we noted above it may be that mean-field theory does not provide a quantitatively reliable description of them. On the other hand, the results for the 8/92 sample are very good for large L.

If, as previous theoretical work and consequent experimental analyses have suggested, the force varies as a power of surface separation, then the data should lie along a straight line on Figure 19. It is clear that this is the case for neither the experimental points nor our theoretical results, except over very limited ranges of L.

By contrast, on the semilogarithmic plot of Figure 20 the theoretical and experimental results are nearly straight

lines over the full range of L, implying that the forces are very nearly exponential functions of surface separation. The slight deviation from simple exponential behavior can be used to make a further theoretical–experimental comparison. Looking first at the theoretical curves, for the 18/90 case there is nonzero curvature, which is positive at small L and changes to negative at $L \simeq 35$ nm. For the 8/92 case the curvature is nearly zero for small L, becoming negative at $L \simeq 60$ nm. In the experimental results, for the 18/90 sample the curvature appears to change from positive to negative at $L \simeq 40$ nm, and for the 8/92 sample, it is at least very close to zero for small L, probably becoming negative at $L \simeq 60$ nm. Even for this good solvent system, where one might have expected mean-field theory to be inadequate, the detailed shapes of the force curves agree to within the experimental error.

Turning to the Θ and slightly worse than Θ solvents, the experimental results of Hadziioannou et al.[4] are reproduced in Figures 21 and 22. As mentioned, the system consisted of PV2P-*b*-PS diblock copolymers and cyclohexane, with tightly adsorbed PV2P blocks. The number-average degree of polymerization of the PS was 580, with polydispersity estimated to be $\bar{M}_W/\bar{M}_N \simeq 1.09$. In the calculations we chose $Z = 580$ and again ignored polydispersity. The average area per polymer was estimated to be $\Sigma \simeq 43$ nm^2, on the basis of the assumption that the PV2P was densely packed on each surface and further that each PV2P block adsorbed as a fully collapsed sphere. It should be noted that the detailed results depend on this assumption: if the adsorbed copolymer layer was more complicated (e.g., bilayers) or if the adsorption was not complete (e.g., micelles remaining in solution), then this could of course affect the measurements.

Finally, we need to know χ, which was not directly measured in the experiments. However, cyclohexane is a Θ solvent for PS at temperature $T_\Theta = 34.5$ °C, and the experiments were done at $T = 38$ °C, which is 3.5 °C above T_Θ, and at $T = 23$ °C, which is 13.5 °C below T_Θ. We have, therefore, explored the regime of $\chi \simeq 0.5$.

Figure 21 compares the calculations with the experimental results for temperature just above T_Θ. For this calculation we choose $\chi = 0.5$, corresponding to a slightly better than Θ solvent for finite molecular weight. The calculation predicts the onset of the force to occur at $L_{max} \simeq 45$ nm, compared with the experimental value of about 30 nm. At smaller separations, the calculated curve passes through the experimental points.

Figure 22 shows the experimental and theoretical results for the same system, but at the lower temperature. Since we know only that this is a slightly bad solvent, we show results for three reasonable values of χ slightly above the value of 0.52 for which the attractive well first appears. The curve with $\chi = 0.54$ gives the overall depth and location of the minimum in very good agreement with experiment, but the repulsive region is a little too far out. Increasing χ slightly to 0.55 gives good agreement in the repulsive region ($L \lesssim 30$ nm), at the expense of deepening the attractive region. In each case there is some disagreement between our results and the experiments at large separation; in the experiments a weak attraction appears to extend out to long range. In fact, the range of the measured force is greater than that in the slightly better than Θ solvent. This suggests the possibility of a more complicated structure of the adsorbed molecules or possibly bridging.

4.4. General Force Curves and Scaling in Near-Θ Solvents. In this subsection we focus on the force curves

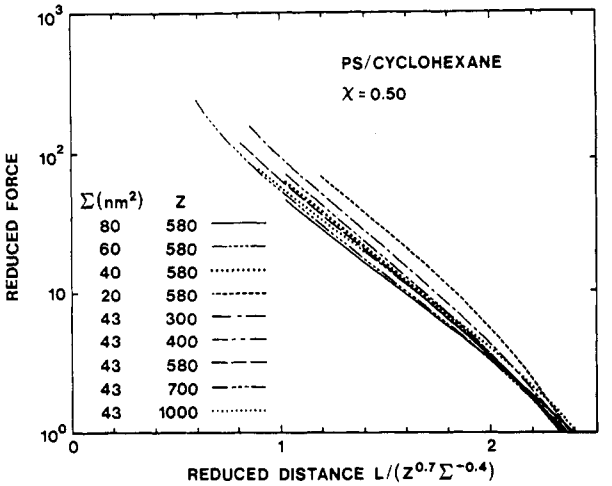

Figure 23. Reduced force, g, as a function of reduced surface separation, as defined in eq 4.1, for the model system with $\chi = 0.5$. Each curve represents the rescaling of the calculated force curve for the case shown.

for the particular case of $\chi = 0.5$. We extract a function that can be used to predict approximately the force curve for a range of Z and Σ. We discuss the scaling of the range of the force and thickness of the brush with Z and Σ and a procedure for determining the brush thickness from the measured L_{max}. Finally, we use our scaling relations to map our calculations onto other cases studied experimentally.

We begin by noting that there can be no universal function that describes exactly all the force curves, even for a particular solvent quality. This follows, for example, from the observation that the brush thickness, as characterized by either $\langle x^2 \rangle^{1/2}$ or x_{max}, does not scale simply with Z or Σ; the appropriate powers vary. Since the range of the force is related to the thickness of the brush, this in turn implies that it does not scale simply with Z or Σ. Therefore, except in the limits of very high or very low coverage, we cannot expect to find universal scaling relations for L_{max}. It follows that there can be no function describing *exactly* all the force curves.

We have found, however, an approximate description of these forces that is valid for a limited, but fairly extensive, range of conditions. We did not assume a particular functional form; instead, we decided to look for a function, labeled g, that would give an approximate description of the force curves via

$$\frac{F}{R} = \frac{Z^\alpha}{\Sigma^\beta} g\left(\frac{L}{Z^\gamma \Sigma^\delta}\right) \tag{4.1}$$

and to calculate g and corresponding powers that gave the best description of the force curves. We found that, for the regime $\Sigma \lesssim 0.3\Sigma_C$, the best values of the exponents are $\alpha = 1.4$, $\beta = 1.0$, $\gamma = 0.7$, and $\delta = -0.40$. The degree to which this function is universal for this range is indicated in Figure 23, which is constructed by inverting eq 4.1 for each force curve listed. If eq 4.1 defined a completely general function g, then all the curves of Figure 23 would coincide exactly. For the various force curves mapped onto Figure 23, Z ranges from 300 to 1000, Σ varies from 20 to 80 nm^2, and the range of the force varies from about 25 to 95 nm. For these cases, Σ/Σ_C varies by a factor of 4, from 0.07 to 0.28. Note that this does not include all our calculated force curves for $\chi = 0.5$; those cases corresponding to less surface coverage than $\Sigma < 0.3\Sigma_C$ had to be excluded. It is also clear that these exponents do not apply to the case of much higher coverage (e.g., $\gamma \to 1$ for $\Sigma/\Sigma_C \ll 1$), although we did not

calculate this limitation quantitatively.

From Figure 23 we see that g, and hence each force curve, has the same qualitative shape as the force curves in the good solvent case, PS/toluene; i.e., g is approximately an exponential function of its argument.

The dependence of the force on Z and Σ as summarized by eq 4.1 implies that care must be taken in relating the measured range of the force to the thickness of the polymer profiles. If we define L_{max} as the separation at which the force vanishes, then it is given by

$$g\left(\frac{L_{max}}{Z^{\gamma}\Sigma^{\delta}}\right) = 0 \tag{4.2}$$

This cannot be solved exactly. However, to the extent that g is universal, eq 4.2 implies that L_{max} scales as

$$L_{max} \propto Z^{\gamma}\Sigma^{\delta} \simeq Z^{0.7}/\Sigma^{0.4} \tag{4.3}$$

for these values of γ and δ.

This result, in particular, the scaling with molecular weight, would appear to contradict interpretations of experiments, which indicated that L_{max} scales linearly with Z. This apparent contradiction can be resolved as follows. Suppose that the range of the force was identified as the separation at which the force first reaches a certain value F_0, for example, corresponding to a threshold value for measurement. In this case the range, which we label $\tilde{L}_{max}$, would be defined by

$$F(\tilde{L}_{max}) = F_0 \tag{4.4}$$

or, using eq 4.1

$$\frac{Z^{\alpha}}{\Sigma^{\beta}}g\left(\frac{\tilde{L}_{max}}{Z^{\gamma}\Sigma^{\delta}}\right) = F_0 \tag{4.5}$$

Next, recall from Figure 19 that, over limited ranges of surface separations, the force curves appear to obey approximate power laws; i.e., $F \propto L^{-p}$. Combining this with eq 4.5 implies that $\tilde{L}_{max}$ scales as

$$\tilde{L}_{max} \propto Z^{\gamma+\alpha/p}\Sigma^{\delta-\beta/p} \tag{4.6}$$

The important point is that $\tilde{L}_{max}$ scales differently than does L_{max}. For example, for both the 18/90 and 8/92 samples, at large L the force varies approximately as L^{-6}, so $p \simeq 6$, which gives (approximately)

$$\tilde{L}_{max} \propto Z/\Sigma^{0.6} \tag{4.7}$$

using our calculated values of α, β, γ, and δ. Equation 4.7 agrees with the original interpretation of experiments, i.e, the linear dependence on Z.

Thus the *scaling* dependence of the range of the force depends on the definition used and, for the second definition discussed above, on the functional form assumed for the force. Both definitions of the range of the force are reasonable. However, to relate the measured force to the thickness of the adsorbed layer (either the rms thickness or x_{max}), we suggest that the definition given in eq 4.2 should be used. In practice this is easily accomplished by examining measured force curves on a semilogarithmic plot.

Although these scaling results have been determined explicitly only for the case $\chi = 0.5$, their general form can be used to understand other experiments. As mentioned in the Introduction, Taunton et al. measured the forces for terminally anchored PS chains in toluene and xylene.[5-7] In one set of experiments,[5] the degree of polymerization of the PS was $Z = 1250$ with polydispersity ratio $\bar{M}_W/\bar{M}_N = 1.02$. The surface coverage was measured to be 3 ± 0.5 mg m^{-2}, which corresponds to $\Sigma = 78$ nm^2 in our notation. Their measured force curves are the same shape as found, for example, by Marra and Hair[9] and as we find theoretically, Figure 20, with an onset at $L = 130 \pm 10$ nm. There was no measurable difference in the force curve when toluene was substituted for xylene.

In order to map our numerical results for the other cases onto this case, we first obtain the appropriate scaling exponents. Since this is a good solvent, $\Sigma_C \simeq 7000$ nm^2. Combining this with the reported value for Σ gives $\Sigma/\Sigma_C \simeq 0.02$. This is well into the limit $\Sigma/\Sigma_C \ll 1$, and so $L_{max} \propto Z^{\gamma}$ with γ very close to unity. Using this to scale the theoretical curve for the 8/92 sample gives for this case $L_{max} \simeq (1250/890)85$ nm $\simeq 120$ nm, which is just within the experimental error. Inclusion of polydispersity would presumably slightly increase the calculated L_{max}.

In other measurements on PS chains in toluene and xylene, they used five different degrees of polymerization ranging from about 250 to 6000.[7] They found that the range of the force scaled approximately as $Z^{0.6}$ (except for the highest molecular weight case) and attributed the relatively slow increase with Z to changes in the surface coverage, i.e., to Σ^{-1} in our notation. However, our results suggest that there is an additional effect, particularly toward the low molecular weight end. For the case $Z \simeq 250$, they estimated $\Sigma \simeq 80$ nm^2, giving $\Sigma/\Sigma_C \simeq 0.2$. This is well below the high-coverage limit, and on the basis of our numerical work as displayed in Figure 23 and Table II, in this range we would expect that $L_{max} \propto Z^{\gamma}$ with $\gamma \lesssim {}^2/_3$ even if there were no variation in Σ.

Ansarifar and Luckham[8] measured force curves for three sets of PV2P-*b*-PBS copolymers in toluene at temperature $T = 22 \pm 2$ °C. The PV2P blocks adsorb onto the surface, with the PBS blocks extending into the good solvent toluene. The weight-average molecular weights of the copolymers were 33 000, 21 400, and 6200, with the corresponding PBS blocks having $\bar{M}_W = 30\,700$, 15 100, and 4700, respectively. They found exponential force curves, with the onset of the force scaling as $L_{max} \propto Z_{PBS}^{0.7}$, which is consistent with our prediction for relatively low molecular weight blocks. They also included the data of Hadziioannou et al.,[4] concluding that both sets of measurements, which extend over 2 orders of magnitude in degree of polymerization, are consistent with this scaling.

We end here by discussing the force measurements of Marra and Hair using high molecular weight PEO-*b*-PS copolymers.[9] In this case $Z_{PS} \simeq 2400$, $\Sigma = 190 \pm 40$ nm^2, and the force was measurable out to $L \simeq 190$ nm. When this is compared with the 18/90 sample for which the force was measurable to $\simeq 60$ nm, it appears that the range of the force increased by a *larger* factor than did the degree of polymerization. This can be understood by recognizing that this characterization of the range of the force is what we have called $\tilde{L}_{max}$ and that, in this experiment, $\Sigma/\Sigma_C \simeq 0.03$, which corresponds to the high-coverage limit. In this regime $L_{max} \propto Z^{\gamma}$ with γ approaching unity; the results summarized in Table II suggest $\gamma \simeq 0.9$. Taking the other exponents as given for eq 4.6 gives (approximately) $L_{max} \propto Z^{0.9}/\Sigma^{0.4}$ and $\tilde{L}_{max} \propto Z^{1.2}/\Sigma^{0.5}$, faster than linearly in Z. Applying this to the measured force curves gives $\tilde{L}_{max}$ for the 20/250 case to be about 3.3 times greater than that for the 18/90 case, in agreement with what was found.

4.5. Polymer Profiles between Two Surfaces. Effects of Compression. Figures 24 and 25 show changes

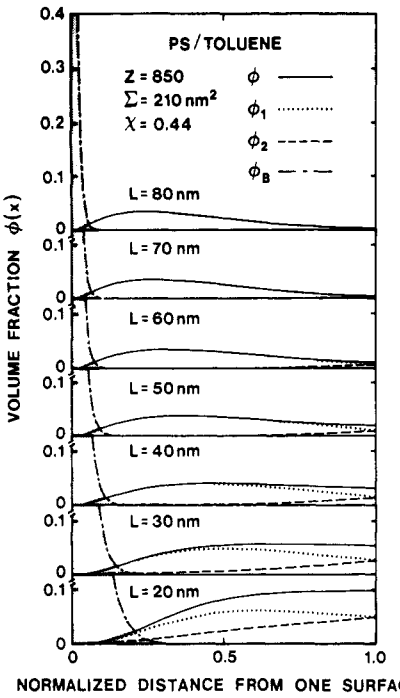

Figure 24. Polymer volume fractions between surfaces as a function of surface separation, L, for the PS/toluene (good solvent) system studied by Marra and Hair,[9] for which we use $Z = 850$, $\chi = 0.44$, and $\Sigma = 210$ nm^2. Each panel corresponds to a different surface separation, L, as indicated. In each case, half of the region between the surfaces is shown and so the horizontal scale differs in each panel. The shaded region at the left-hand side represents the outer part of the adsorbed PEO block of the copolymer falling smoothly from unity to zero. The solid line reprsents the total PS volume fraction, $\phi(x)$, at each point. The two contributions to it, $\phi_1(x)$ and $\phi_2(x)$, are shown as dotted and dashed lines respectively. The solvent profile, which is given by $\phi_S(x) = 1 - \phi_{PEO}(x) - \phi_{PS}(x)$, is not shown. The corresponding force curve for this case is shown in Figures 18–20.

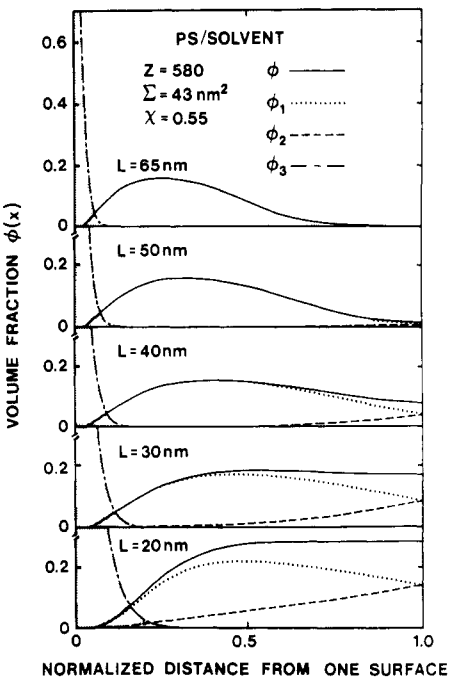

Figure 25. Polymer volume fractions between surfaces as a function of surface separation, for the PS/cyclohexane (bad solvent) system studied by Hadziioannou et al.,[4] for which we use $Z = 580$, $\chi = 0.55$, and $\Sigma = 43$ nm^2. Each panel corresponds to a different surface separation, L, as indicated. The notation is described in Figure 24, except that the tightly adsorbed block in this case is PV2P. The corresponding force curve for this case is shown in Figure 22.

in the polymer profiles as the surfaces are brought together. The first of these figures is for the good solvent case, PS/toluene, with $Z = 850$, $\chi = 0.44$, and $\Sigma = 210$ nm^2; the corresponding force curve for this case is shown in Figures 18–20. Figure 25 is for a worse than Θ solvent, PS/cyclohexane, with $Z = 580$, $\chi = 0.55$, and $\Sigma = 43$ nm^2; the corresponding force curve for this case is shown in Figure 22. Results for the Θ solvent case are qualitatively similar and so are not shown.

In each panel of these figures, half of the region between the surfaces is shown. The shaded profile on the left represents the outer part of the tightly adsorbed B block of the copolymer. The solid line represents the total volume fraction of the dangling block, $\phi(x)$. The two contributions to it, $\phi_1(x)$ and $\phi_2(x)$, are shown as dotted and dashed lines, respectively.

Consider Figure 24 first. The top panel corresponds to a surface separation of $L = 80$ nm; at this large separation the brushes attached to opposite surfaces do not reach each other. Hence, in the half region shown, $\phi(x) = \phi_1(x)$, and $\phi_2(x)$ is zero. The effects of reducing L are shown in successive panels. In the second and third panels, for which $L = 70$ and 60 nm, the most obvious change is that the two distributions begin to overlap in the center; i.e., the tail from $\phi_2(x)$ penetrates into the tail of $\phi_1(x)$ and vice versa. As L is further reduced, this penetration increases, until, at $L \simeq 40$ nm, each profile reaches fully across the region. With decreasing separation, the polymer density at the midpoint increases continuously, and for $L \simeq 30$ nm the total density is nearly uniform, except for the two depletion regions near the surfaces. As L is further reduced, the polymer density exhibits a broad maximum at the center.

Figure 25 shows a similar progression for the poor solvent, $\chi = 0.55$. In this case the polymer density is greater than that in the previous case, but qualitatively the results are similar. The point to note in particular is that in our calculations the two distributions greatly interdigitate. As the surface separation decreases to $L \simeq 30$ nm, each profile reaches fully across to the opposite surface, and the total PS profile is nearly constant throughout the interior.

Pursuing the analysis further, we relate the polymer profiles to the force at various separations L, first for the good solvent case. From Figure 18, the onset of the force occurs at $L \simeq 60$ nm. From Figure 24 we see that even at this separation the opposing layers interdigitate. When L is reduced to about 30 nm, such that each profile reaches fully across to the opposite surface, F/R is only 500 mN m^{-1}. This is a relatively small force on the scale of these measurements, in which F/R rises to more than 10 times this value at $L \simeq 12$ nm. For all surface separations less than about 30 nm, the polymer density has a broad maximum at the center, as identified above. This contrasts with models in which the density is assumed to be zero at the midpoint when calculating the force.

We noted earlier that out calculations underestimate the range of the force for this case by about 10 nm but that this could probably be corrected by including, for example, polydispersity. If we were to do so, then at each separation L we would find even more interpenetration. Thus the calculations unambiguously predict considerable interpenetration at virtually every separation for which the force is measurable.

For the worse than Θ solvent case we use the calculations for PS/cyclohexane, Figures 9, 14, 22, and 24, for $\chi = 0.55$. Note first from Figures 14 and 22 that the onset of the force for this case occurs at about 55 nm.

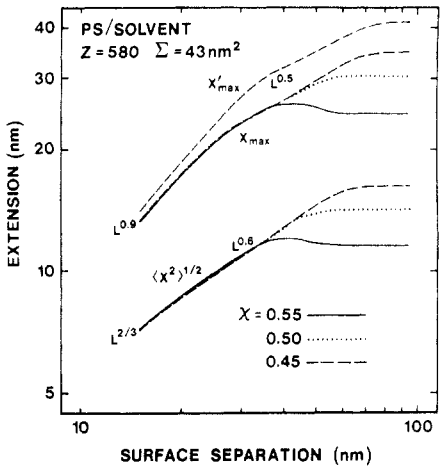

Figure 26. Root-mean-squared thickness of each profile, $\langle x^2\rangle^{1/2}$, and maximum extent of each profile as measured by x_{max}, as a function of surface separation for the model system for χ = 0.45, 0.5, and 0.55. For the good solvent case, χ = 0.45, we also show x'_{max}; the region between x_{max} and x'_{max} contains 0.9% of the profile.

From Figure 9 we see that a single profile extends to about 32 nm, and from this and from Figure 24, it is clear that at $L \simeq 55$ nm the profiles interdigitate. Thus, as before, for all measurable values of the force the opposing profiles interdigitate. As L is further reduced, the profiles fully interpenetrate. In fact, in this case the force is most attractive at $L \simeq 35$ nm, at which separation each profile has reached nearly all the way across. For all $L \lesssim$ 30 nm, which is the entire range through which the force is repulsive, each profile fully traverses the region.

As well as interdigitating, as the surfaces are brought together the profiles retract, but more slowly than is implied by the linear scaling assumed by AdeG and MWC. In Figure 26 we illustrate this quantitatively by plotting $\langle x^2\rangle^{1/2}$ and x_{max} for each layer as a function of surface separation. In order to make direct comparison, for this figure we use the PS/cyclohexane system with Z = 580, Σ = 43 nm^2, and three values of χ, namely 0.55, 0.5, and 0.45. The first of these is the same as that of Figure 24, and the third is qualitatively the same as the good solvent case of Figure 25.

Qualitatively, the results for the two cases χ = 0.45 and 0.5 are similar. For large L, both the rms layer thickness and x_{max} are constant, with the profile in the better solvent being further extended, $\langle x^2\rangle^{1/2}$ = 16 vs 14 nm and x_{max} = 35 vs 30 nm. As the surfaces are brought together, when the tails of the opposing profiles touch, they begin to withdraw. Initially $x_{max} \propto L^{1/2}$ and $\langle x^2\rangle^{1/2} \propto L^{0.6}$, but as the surfaces are brought closer together, x_{max} in particular begins to decrease more quickly, reaching $x_{max} \propto L^{0.9}$ in our calculations. Since $x_{max} < L$ always, this much approach a limit of linear scaling at small L. For the smallest case shown, L = 15 nm, x_{max} = 13.3 nm, and we have almost reached this limit. By contrast, at this point $\langle x^2\rangle^{1/2}$ is still varying only as $L^{2/3}$.

For the bad solvent case there is an additional effect, occurring when the surface separation equals about twice the size of a single adsorbed profile. Initially, $x_{max} \simeq 25$ nm and $\langle x^2\rangle^{1/2} \simeq 11.5$ nm, but as the surfaces are brought together from $L > 60$ nm, the individual profiles first *expand* and interdigitate. As the surfaces come closer together, the profiles then begin to contrast, returning to their original thickness at $L \simeq 33$ nm. This is very close to the separation at which the force is most attractive. It also corresponds to the separation at which each profile first reaches to the opposite surface. As L is further reduced, the profile is further compressed, and the force becomes repulsive.

For all separations $L \lesssim 35$ nm, both x_{max} and $\langle x^2\rangle^{1/2}$ depend only on the surface separation and are independent of solvent quality. This is the case even though they are not being squeezed very much in this regime; both x_{max} and $\langle x^2\rangle^{1/2}$ are much smaller than the surface separation and scale more slowly than linearly with L (except for very small separation).

The exact behavior of x_{max} depends on its definition. To illustrate this, we have included x'_{max} in Figure 26 for the case χ = 0.45 (x'_{max} contains 99.9% of the profile). For large surface separation, $x'_{max} \simeq 40$ nm, compared with $x_{max} \simeq 35$ nm. It begins to decrease at $L \simeq$ 90 nm, which is very close to the range of the force. This compares with the significantly smaller surface separation of about 70 nm at which x_{max} begins to decrease. The detailed variations of x_{max}, x'_{max}, and $\langle x^2\rangle^{1/2}$ with L reflect changes in the size and shape of the profiles, including the tail, as the surfaces come together.

We end this section with one additional comment. As per the above discussion, as L decreases different parts of the brush deform differently, for example $\langle x^2\rangle^{1/2}$, x_{max}, and x'_{max} scale with differing powers. This result should apply as well to the case of a single polymer brush compressed by a hard wall and should be included when calculating the free energy of a compressed polymer brush.

5. Summary

In this paper we have studied adsorbed diblock copolymers in systems where the solvent is very bad for one of the blocks and either a good, Θ, or poor solent for the second block. The primary interest has been the dangling block; the model applies equally well to the problem of chains grafted to the surface.

The basis of the work is the full numerical solutions to the mean-field self-consistent equations describing polymer/solvent and polymer/polymer blends.[21-28] The approximations inherent to mean-field theory limit its range of applicability, particularly for low concentrations of polymer in a good solvent. For this reason, we have restricted our attention to "near"-Θ conditions, with the Flory χ parameter restricted to $\chi \simeq 0.5$. We have, however, intentionally explored the limits of this regime, with χ as low as 0.4 in some cases and very low surface coverage in others. We have also made detailed comparisons with experiment, using independently determined values for the Kuhn statistical length, monomer and solvent molecule volumes, and interaction (χ) parameters. Most of our results have been presented in sections 3 and 4 of this paper. Here we revisit the main conclusions that we have drawn.

We first reported a series of model calculations, studying the ranges $200 \le Z \le 1000$, 20 nm$^2 \le \Sigma \le 400$ nm^2, and $0.4 \le \chi \le 0.6$. In all cases, the polymer profiles rise from zero to a maximum, ϕ_{max}, which is a finite distance from the surface. This is followed by a decrease, which is initially approximately parabolic but evolves into a smooth, extended "tail". The initial rise is analogous to the depletion layer discussed by de Gennes,[11-13] but in our calculations its thickness, as measured by the location of ϕ_{max}, is almost independent of the average surface area per molecule, Σ. Instead, it depends weakly on the degree of polymerization of the dangling blocks and on the solvent quality. The decrease in $\phi(x)$ following ϕ_{max} is similar to the parabolic profile predicted by Milner, Witten, and Cates.[15-18] However, the extended tail is nonnegligible for all cases.

For progressively better solvents, the layer becomes thicker and ϕ_{max} becomes correspondingly smaller. The value of ϕ_{max} depends on all of Z, Σ, and χ. However, for a given solvent quality, the dependence on Z and Σ appears to saturate in the limit of high Z and/or low Σ, as predicted by the models of AdeG and MWC. The saturation is apparently reached earliest in the good solvent, the case to which the AdeG and MWC models are applied. The value of ϕ_{max} does not vary with either χ or the excluded-volume parameter, w, as a simple power law or exponential function.

For good and Θ solvents, the dependence of the layer thickness on Z and Σ appears to vary smoothly from the limits of Z^{ν}/Σ^{0} for low surface coverage toward $Z^{1}/\Sigma^{1/3}$ for high surface coverage. This applies to both the rms thickness and the total thickness including the tail. Similarly, the dependence of the maximum polymer density appears to vary from $Z^{1-\nu}/\Sigma$ for low surface coverage toward $Z^{0}/\Sigma^{2/3}$. We have concluded that experiments that have been done to date lie in different regimes within these limits. In only one of the cases that we have examined would we expect the layer thickness to scale linearly with Z.

For poor solvent, there is a nonmonotonic dependence of layer thickness of Σ; in circumstances of intermediate coverage, the layer thickness *decreases* with increasing coverage (e.g., decreasing Σ). Although a quantitative treatment of this effect is outside the scope of our calculations, we suggest that it is an interesting effect to look for experimentally, perhaps using small-angle neutron scattering.

We found the calculated long-range forces to be qualitatively similar for Θ and good solvents, with the range of the force increasing with improving solvent quality. For poor solvent there is a qualitative difference, with an attractive region appearing.

We have made detailed comparisons with experiment for good solvent ($\chi \simeq 0.44$), near-Θ solvent, and poor solvent ($\chi \simeq 0.55$) conditions. Given the experimental uncertainty, in particular, in the determination of Σ, and the neglect in the calculations of polydispersity and the possible concentration dependence of χ, the agreement appears to be satisfactory except in some cases for relatively large surface separations. We conclude that mean-field theory is adequate for these systems at least over the tested range $0.45 \leq \chi \leq 0.55$, although it may provide only a qualitative description of the tail.

We argued that, even for a given polymer/solvent pair, there can be no universal force curve or scaling laws. However, for the particular case $\chi = 0.5$, we found an approximate function that can be used to quantitatively predict the force curve for a range of Z and Σ, which can be specified in terms of the ratio Σ/Σ_C, where $\Sigma_C \simeq Z^{2\nu}b^2$. From this function we concluded that, in order to map from one system to another, both the surface separation *and* the magnitude of the force must be rescaled.

This function implies approximate scaling laws for the range of the force, applicable up to $\Sigma/\Sigma_C \simeq 0.3$, but that care must be taken in relating the range of the force to the thickness of a polymer layer. In particular, if the range is defined to be the distance at which the force equals a certain value, such as a threshold for measurement, then it scales faster with Z than does the layer thickness, characterized by either $\langle x^2\rangle^{1/2}$ or x_{max}. For high molecular weight chains, this apparent range of the force can increase more quickly than as a linear function of Z, as observed by Marra and Hair.[9]

The calculations provide a detailed picture of the changing profiles in the surface force apparatus. In good and Θ solvents, as the surface separation L is reduced the profiles interpenetrate, partially retract, and deform. Initially, the thickness of each layer varies approximately as $L^{1/2}$. As L is further reduced, the thickness decreases more quickly, approaching $x_{max} \propto L$. However, the rms thickness decreases more slowly; over the range of our calculations it scales no faster than $\langle x^2\rangle^{1/2} \propto L^{2/3}$, even for rather highly compressed brushes. This relatively slow retraction of the brushes is consistent with the interdigitation and deformation of the profiles. The interdigitation is apparent for all surface separations for which the forces are measurable. In fact, except for the outer range of the force curves, each profile reaches fully across to the opposite surface, and the polymer density exhibits a broad maximum at the center of the region. This picture contrasts with models in which the force is calculated by ignoring interdigitation, thereby assuming that the density vanishes at the midpoint between the surfaces and that each individual brush thickness is proportional to L. The continuous deformation of the brush should also be included in modeling the compression of a brush by a hard wall.

In worse than Θ solvent we have predicted an additional effect which is similar to the nonmonotonic dependence of layer thickness of Σ. As the surface separation is reduced, when the tails of the opposing brushes first approach one another, the layers extend and interpenetrate. As L is further reduced, they then begin to retract. In this case, we found that the attractive region of the force curve correlates with the expanded brushes, and the repulsive part (in all solvents), with the compressed brushes.

Acknowledgment. We thank L. Marks for assistance in developing the mathematical techniques and computer programs for solving the self-consistent diffusion equations and M. Hair, T. Kavassalis, and M. Tirrell for useful discussions. M. Whitmore thanks the Xerox Research Centre of Canada for hospitality during the course of much of this work. The work is supported in part by the Natural Sciences and Engineering Research Council of Canada.

Appendix

Self-Consistent Solution of Diffusion Equation. We need to solve partial differential equations for $q_0(x,t)$, $q_1(x,t)$, and $q_2(x,t)$, subject to appropriate initial and boundary conditions and find the self-consistent mean-field potential, $w_A(x)$. The problem is specified by eqs 2.3, 2.5, and 2.7–2.16.

Rescaling. The equations are scaled so that $x\epsilon[0,L]$ is mapped onto $y\epsilon[0,\pi]$ and $t\epsilon[0,Z_A]$ is mapped onto $\tau\epsilon[0,1]$. (This transformation is the same as that used in ref 39.) The distribution functions then satisfy

$$\frac{1}{T}\frac{\partial}{\partial\tau}q_i = \left[\frac{\partial^2}{\partial y^2} - w^*\right]q_i \tag{A.1}$$

where

$$T = Z_A\pi^2 b_A^2/6L^2 \tag{A.2}$$

and

$$w^*_A(y) = (Z_A/T)w_A(x) \tag{A.3}$$

The initial conditions become

$$q_0(y,0) = 1$$

$$q_1(y,0) = \theta\left[\frac{a\pi}{L} - y\right]$$

$$q_2(y,0) = \theta\left[y - \pi\left(1 - \frac{a}{L}\right)\right] \quad \text{(A.4)}$$

with boundary conditions:

$$q_i(0,\tau) = q_i(\pi,\tau) = 0 \quad \text{(A.5)}$$

The convolutions are appropriately modified; eq 2.14 becomes

$$\phi_{Ai}(y) = \frac{\bar{\phi}_A}{2\langle q_1(1)\rangle}\int_0^1 q_i(y,\tau)\, q_0(y,1-\tau)\, d\tau \quad \text{(A.6)}$$

Solution of Diffusion Equation. We use an iterative procedure to achieve a self-consistent solution. At each iteration, we have a function w^*_A for which the differential equations are solved via eigenfunction expansions

$$q_i(y,\tau) = \sum_m a_{im} e^{-\lambda_m T\tau} f_m(y) \quad \text{(A.7)}$$

where the λ_m and f_m are found from the ordinary differential equation

$$\left[-\frac{d^2}{dy^2} + w^*_A(y)\right] f(y) = \lambda f(y) \quad \text{(A.8)}$$

subject to

$$f(0) = f(\pi) = 0 \quad \text{(A.9)}$$

The three sets of expansion coefficients are determined from the initial conditions. The potential w^*_A is symmetric, so the eigenfunctions are either symmetric or antisymmetric. For constructing ϕ_A, only the symmetric eigenfunctions are needed, which are computed on $[0,\pi/2]$. This interval is subdivided into N subintervals specified by a set of points that are densely spaced near the logarithmic singularity at $y = 0$. We use the set

$$y_i = \frac{\pi}{2}\frac{e^{\alpha u_i} - 1}{e^{u_i} - 1} \quad \text{(A.10)}$$

where u_i is a uniform net of N equal intervals on [0, 1] and $\alpha = 2.5$. Depending on L, we use N equal to 200 or 400. The potential w^*_A is modeled as a piecewise constant function on the subintervals $[y_i,y_{i+1}]$. In each subinterval, the solution of eq A.8 is a linear combination of two circular or two hyperbolic functions with two multiplicative constants. Taking the solution in the first interval as either a sine or hyperbolic sine function in order to satisfy the boundary condition at $y = 0$, then the constants are determined in succession by imposing the continuity of the solution and its derivatives at each point y_i. The eigenvalues, λ_m, must be determined so that

$$f'(y,\lambda_m)\big|_{y=\pi/2} = 0 \quad \text{(A.11)}$$

We require an efficient method of searching for the first M-ordered eigenvalues, λ_m. It is useful to introduce the Prüfer transformation:[44,45]

$$f(y,\lambda) = \rho(y,\lambda)\sin\theta(y,\lambda)$$

$$f'(y,\lambda) = \rho(y,\lambda)\cos\theta(y,\lambda) \quad \text{(A.12)}$$

In particular the phase angle $\theta(y,\lambda)$ associated with any solution $f(y,\lambda)$, where λ is arbitrary, is computable from $f(y,\lambda)$. It is a monotonically increasing function of λ for all $\lambda\epsilon(-\infty,\infty)$. We determine λ_m by solving

$$\theta(\pi/2,\lambda_m) = (2m-1)\pi/2 \quad \text{(A.13)}$$

for $m = 1,2, \ldots, M$. Then f_m is the mth symmetric eigenfunction of the problem, and λ_m is the corresponding eigenvalue. For sufficient precision in our calculated $E(L)$, we find that eq A.13 must be solved with an error of less than 10^{-8}. For large Z_A and L, we must include up to $M = 2500$ eigensolutions.

Once the eigenvalue problem is solved, we construct the $\phi_A(y)$ via eq A.6, which becomes

$$\phi_A(y) = \frac{\pi}{2}\frac{\bar{\phi}_A}{2}\frac{\sum_{j,k=1}^{M} a_{1j}a_{0k}\dfrac{e^{-\lambda_j T} - e^{-\lambda_k T}}{T(\lambda_k - \lambda_j)} f_j(y)\, f_k(y)}{\sum_{j=1}^{M} a_{1j}a_{0j}e^{-\lambda_j T}} \quad \text{(A.14)}$$

The convergence of this double sum is controlled by both the exponential terms and the factor $1/[T(\lambda_k - \lambda_j)]$. The summation is reduced greatly by omitting terms where both $e^{-\lambda_j T}$ and $e^{-\lambda_k T}$ are small. For example, if $M = 1000$ the double sum has 10^6 terms, but only about 1000×20 are nonnegligible.

Self-Consistency. For a given Z_A and L, we begin the calculation with an initial estimate of $\phi_A(y)$, say, $\phi^1{}_A(y)$. Starting with $\phi^1{}_A = 0$ often suffices, but we usually start with the converged solution from another related. From $\phi^1{}_A$ we calculate w^*_A through eqs 2.16 and A.3. We then solve the diffusion equations and calculate a new $\tilde{\phi}^1{}_A(y)$ as described above. In general this $\tilde{\phi}^1{}_A(y)$ is of itself useless, but

$$\phi^2{}_A(y) = \phi^1{}_A(y) + \epsilon[\tilde{\phi}^1{}_A(y) - \phi^1{}_A(y)] \quad \text{(A.15)}$$

with $\epsilon \simeq 0.1$, will in general provide a better estimate. Iterating according to eq A.15, the calculation generally coverges, i.e.

$$\lim_{k\to\infty}[\tilde{\phi}^k{}_A(y) - \phi^k{}_A(y)] = 0 \quad \text{(A.16)}$$

This convergence is slow. Viewing $\tilde{\phi}_A(y) - \phi_A(y)$ as a vector, we can formulate the problem as solving the vector equation $\tilde{\phi}^*_A - \phi^*_A = 0$ (on the points $y = y_i$, $i = 1, \ldots, N$). We use the generalized secant method to reduce the error in $\tilde{\phi}_A - \phi_A$. For example, if $\phi^1{}_A$, $\phi^2{}_A$, $\phi^3{}_A$, and $\phi^4{}_A$ are generated by eq A.15, then $\phi^5{}_A$, derived from the generalized secant method, shows a marked improvement (factor of 10) in the metric separation δ defined by

$$\delta = \max_i[\tilde{\phi}_A(y_i) - \phi_A(y_i)] \quad \text{(A.17)}$$

We terminate the iterations when $\delta < 10^{-7}\bar{\phi}_A$.

References and Notes

(1) Cosgrove, T.; Crowley, T. L.; Mallagh, L. M.; Ryan, K.; Webster, J. R. P. *Polym. Prepr.* **1989**, *30*, 370.
(2) Cosgrove, T.; Heath, T. G.; Phipps, J. S.; Richardson, R. M., submitted for publication in *Macromolecules*.
(3) Killmann, E.; Maier, H.; Baker, J. A. *Colloids Surf.* **1988**, *31*, 51.
(4) Hadziioannou, G.; Patel, S.; Granick, S.; Tirrell, M. *J. Am. Chem. Soc.* **1986**, *108*, 2869.
(5) Taunton, H. J.; Tropakcioglu, C.; Fetters, L. J.; Klein, J. *Nature (London)* **1988**, *332*, 712.
(6) Taunton, H. J.; Toprakcioglu, C.; Fetters, L. J.; Klein, J. *Colloids Surf.* **1988**, *31*, 151.
(7) Taunton, H. J.; Toprakcioglu, C.; Fetters, L. J.; Klein, J. *Polym. Prepr.* **1989**, *30*, 368.
(8) Ansarifar, M. A.; Luckham, P. F. *Polymer* **1988**, *29*, 329.
(9) Marra, J.; Hair, M. L. *Colloids Surf.* **1988–89**, *34*, 215.
(10) Alexander, S. *J. Phys. (Les Ulis, Fr.)* **1977**, *38*, 983.
(11) de Gennes, P.-G. *Macromolecules* **1980**, *13*, 1069.
(12) de Gennes, P.-G *Adv. Colloid Interface Sci.* **1987**, *27*, 189.
(13) de Gennes, P.-G. *Ann. Chim.* **1987**, *77*, 389.
(14) Patel, S.; Tirrell, M.; Hadziioannou, G. *Colloids Surf.* **1988**, *31*, 157.

(15) Milner, S. T.; Witten, T. A.; Cates, M. E. *Europhys. Lett.* **1988**, *5*, 413.
(16) Milner, S. T.; Witten, T. A.; Cates, M. E. *Macromolecules* **1988**, *21*, 2610.
(17) Milner, S. T.; Wang, Z.-G.; Witten, T. A. *Macromolecules* **1989**, *22*, 489.
(18) Milner, S. T.; Witten, T. A.; Cates, M. E. *Macromolecules* **1989**, *22*, 853.
(19) Milner, S. T. *Europhys. Lett.* **1989**, *7*, 695.
(20) Whitmore, M. D.; Noolandi, J. APS March Meeting, Las Vegas, 1986; APS March Meeting, New York, 1987.
(21) Hong, K. M.; Noolandi, J. *Macromolecules* **1981**, *14*, 727.
(22) Hong, K. M.; Noolandi, J. *Macromolecules* **1983**, *16*, 1083.
(23) Noolandi, J.; Hong, K. M. *Polym. Bull.* **1982**, *7*, 561.
(24) Edwards, S. F. *Proc. Phys. Soc. London* **1965**, *85*, 613.
(25) Dolan, A. K.; Edwards, S. F. *Proc. R. Soc. London* **1975**, *A343*, 427.
(26) Helfand, E. *Macromolecules* **1975**, *8*, 552.
(27) Helfand, E.; Wasserman, Z. R. *Macromolecules* **1976**, *6*, 879.
(28) Helfand, E.; Wasserman, Z. R. In *Developments in Block Copolymers*; Goodman, I., Ed.; Elsevier: New York, 1982; Vol. 1.
(29) Cosgrove, T.; Heath, T.; van Lent, B.; Leermakers, F.; Scheutjens, J. M. H. M. *Macromolecules* **1987**, *20*, 1692.
(30) Muthukumar, M.; Ho, J.-S. *Macromolecules* **1989**, *22*, 965.
(31) Murat, M.; Grest, G. *Phys. Rev. Lett.* **1989**, *63*, 1074.
(32) Marques, C.; Joanny, J. F.; Leibler, L. *Macromolecules* **1988**, *21*, 1051.
(33) Marques, C. M.; Joanny, J. F. *Macromolecules* **1989**, *22*, 1454.
(34) Munch, M. R.; Gast, A. P. *Macromolecules* **1988**, *21*, 1366.
(35) Theodorou, D. N. *Macromolecules* **1988**, *21*, 1411; *Macromolecules* **1988**, *21*, 1422.
(36) Schaefer, D. W.; Joanny, J. F.; Pincus, P. *Macromolecules* **1980**, *13*, 1280.
(37) Fleer, G. J.; Scheutjens, J. M. H. M.; Cohen Stuart, M. A. *Colloids Surf.* **1988**, *13*, 1.
(38) Deryaguin, B. V. *Kolloid Zh.* **1934**, *69*, 155.
(39) Whitmore, M. D.; Noolandi, J. *Macromolecules* **1988**, *21*, 1485.
(40) Scheutjens, J. M. H. M.; Fleer, G. J. *J. Phys. Chem.* **1979**, *83*, 1619.
(41) Brandrup, J.; Immergut, E. H., Eds. *Polymer Handbook*, 2nd ed.; Interscience: New York, 1975.
(42) Richardson, M. J.; Savill, N. G. *Polymer* **1977**, *18*, 3.
(43) See, for example: Scheutjens, J. M. H. M.; Fleer, G. J. *J. Phys. Chem.* **1980**, *84*, 178; *Adv. Colloid Interface Sci.* **1982**, *16*, 341.
(44) Birkoff, G.; Rota, G. C. *Ordinary Differential Equations*, 2nd ed.; John Wiley and Sons: New York, 1966; pp 288–296.
(45) Hille, E. *Lectures on Ordinary Differential Equations*; Addison-Wesley: London, 1969; pp 394–402.

Polydispersity Effects on the Microphase-Separation Transition in Block Copolymers

C. Burger and W. Ruland*

Universität Marburg, Fachbereich Physikalische Chemie, D-3550 Marburg/Lahn, FRG

A. N. Semenov

Physics Department, M. V. Lomonosov Moscow State University, Moscow 119899, USSR

Received October 27, 1989

ABSTRACT: The influence of polydispersity on the transitions occurring in the weak segregation regime and on the scattering functions of the disordered phase in diblock copolymers is studied for one-component and multicomponent systems including mixtures with homopolymers. Application of the fluctuation corrections given by Fredrickson and Helfand[9] leads to the determination of the transition windows as a function of degree of polymerization N, polydispersity U, and composition f. The applicability of the fluctuation corrections appears to be extended to lower N and f with increasing U. The prediction of transitions is facilitated by the concept of a reduced phase diagram.

1. Introduction

The capability of block copolymers to form microdomain structures is well-known and widely used to produce a variety of polymer materials with outstanding properties. Understanding the basic principles of the microphase separation thus not only is of interest from a purely scientific point of view but is expected to show new ways to improved polymer materials.

Using methods based on the mean-field theory, Helfand and co-workers,[1] Ohta and Kawasaki,[2] and Semenov[3] have been able to make quantitative predictions on the ranges of stability of the one-, two-, and three-dimensionally periodic structures appearing in the strong segregation limit. New developments are expected in this field since recent studies by Thomas and co-workers[4–6] and Hashimoto and co-workers[7] have shown that the shapes of the domains are not restricted to spheres, cylinders, and lamellae.

The transition from the ordered phase-separated structure to the homogeneous melt and the phase diagram in the weak segregation limit is another feature of general interest. According to the theory of Leibler,[8] this phase diagram is, for diblock copolymers, completely defined by the composition f and the product χN, where χ is the Flory–Huggins interaction parameter and N the total number of statistical segments per molecule. A particularity of Leibler's theory is the prediction that, except for $f = 0.5$, there is no direct transition to ordered structures other than the bcc macrolattice.

Recently, Fredrickson and Helfand[9] have extended Leibler's theory to include the effect of composition fluctuations using a method established by Brazovskii.[10] They find that Leibler's theory is only valid in the limit $N \to \infty$ and that direct transitions from the homogeneous melt

* To whom correspondence should be addressed.

0024-9297/90/2223-3339$02.50/0